DTU Library

Acid-Stable and Active M-N-C Catalysts for the Oxygen Reduction Reaction
The Role of Local Structure

Patniboon, Tipaporn; Hansen, Heine Anton

Link back to DTU Orbit

Acid stable and active M-N-C catalysts for the oxygen reduction reaction: the role of local structure

Tipaporn Patniboon, Heine Anton Hansen*

Department of Energy Conversion and Storage, Technical University of Denmark

Anker Engelunds Vej, 2800 Kongens Lyngby, Denmark

*corresponding author: heih@dtu.dk

Abstract

Metal-nitrogen carbon (M-N-C) catalysts; atomically dispersed and nitrogen-coordinated MN_x sites embedded in carbon planes have exhibited encouraging oxygen reduction reaction activity in an acidic environment. However, one challenge for these materials is their insufficient long-term stability in the acid environment. Herein, we systematically investigate both a catalytic activity toward ORR and stability under acid conditions using density functional theory (DFT). Various local atomic structures around the MN_x site and different metal atoms (M=Cr, Mn, Fe, Co, Ni, and Ru) are considered in this study to understand the relation between atomic structures, stability, and catalytic activity. The stability of the M-N-C catalyst is considered from the propensity of the metal atom center to dissolve from the carbon host structure. The calculations reveal that the considered MN_x sites are thermodynamically unstable in acid ORR conditions. However, based on the calculated thermodynamic driving force towards the metal dissolution, the MN_4 site with Fe, Co, Ni, and Ru metal atom embedded on the graphene plane and at the graphene edge are more stable in acid ORR condition than the other considered MN_x structures. Combining stability and catalytic activity descriptor, we propose some acid-stable and active MN_x structures toward ORR. This computational study provides helpful guidance to rational modification of carbon matrix hosting MN_x moieties and appropriate selection of a metal atom for optimizing the activity and stability toward the ORR reaction.

1. Introduction

The proton exchange membrane fuel cell (PEMFC) is a highly efficient clean energy conversion device that requires a highly active catalyst for the oxygen reduction reaction (ORR) at the cathode. Platinum-based catalysts now reach high activity and durability[1]. However, considering the high cost and lack of platinum-based catalysts, the catalyst-free of platinum group remains an alternative catalyst for cost and sustainability reasons.

Among catalysts free of platinum group metals, metal-nitrogen carbon (M-N-C) catalysts, where atomically dispersed and nitrogen-coordinate MN_x sites are embedded in carbon planes, have gained much attention due to their high initial activity toward the ORR in acid media, especially Fe-N-C catalysts[2–4]. However, the issue facing the Fe-N-C catalyst is an insufficiency of long-term stability. The Fe-N-C catalyst tends to degrade quickly in the acidic PEMFC environment[5], but the degradation mechanism remains elusive and further investigations and improvements for the M-N-C catalysts are still needed. However, various degradation mechanisms have been proposed to degrade M-N-C catalysts, such as carbon oxidation by hydroxyl or hydroperoxyl radicals[6,7], demetallation of metal sites[8,9], and carbon corrosion[10].

On top of that, the synthetic approaches that involve pyrolysis of the mixture metal, nitrogen, and carbon precursor often result in the various local environment for the MN_x site[11,12], so the ORR catalytic activity and stability of the M-N-C materials is highly dependent on the synthesis path. Different configurations of the MN_x sites have been proposed as an active site for the ORR by experimental and theoretical studies[13–15], but the specific MN_x sites, which are active and durable under working conditions, should be preferred targets for synthesis. The Fe-N-C catalyst prepared via pyrolysis in flowing NH_3 has been reported to have higher initial ORR activity in acid and alkaline conditions than similarly prepared Fe-N-C pyrolyzed in an inert atmosphere[12,13]. However, the NH_3 pyrolyzed Fe-N-C catalyst results in about 10 times enhanced Fe leaching rate than the inerted gas pyrolyzed catalyst in acid.[12,13] It has been reported that the NH_3 pyrolysis promotes high basicity and porosity in the Fe-N-C catalyst surface[12,13,16]. The introduction of micropores has been suggested to enhance the catalytic activity for ORR[17,18]. In contrast, the initial ORR performance loss has also been proposed due to the demetallation of the FeN_4 site located in the micropore[16]. In addition, a recent experimental study by Li et al. [19] using operando x-ray absorption spectroscopy has reported that there are two types of FeN_4 sites identified in the Fe-N-C catalyst. These are FeN_4C_{10}, and FeN_4C_{12} sites, surrounded by a different local carbon structure. Both sites initially contribute to the ORR activity of the Fe-N-C in an acidic medium. However, the FeN_4C_{12} site is not durable under operation, rapidly converting into inactive ferric oxide particles as there is a decreasing ORR activity, decreasing number of this site, and increasing ferric oxide formation. The FeN_4C_{10} site is stable under the acid condition with no

measurable decrease in the number of this active site after 50h operating at 0.5V[19]. Therefore, the local atomic structures of the MN_x have been suggested to play a significant role in ORR catalytic activity and demetallation of the active site[10,17,19,20].

Besides the Fe-N-C catalyst, the Co-N-C catalyst has been the most investigated as a replacement for Fe since the dissolved Fe ions from the Fe-N-C catalysts can further deteriorate the membrane durability by catalyzing the formation of radicals from H_2O_2, which degrade the membrane[6,21]. Thus, metal atom sites which do not promote the formation of H_2O_2 radicals are also needed. A previous study by Xie et al. has reported that the Co-N-C catalyst has inferior catalytic activity toward ORR and lower activity for promoting radicals from H_2O_2 but has significant resistance to demetallation in acid condition[22]. Since various CoN_x sites can be simultaneously formed during the synthesis[23], specific knowledge of the detailed structures of the active and durable CoN_x site would be valuable. Furthermore, other M-N-C catalysts have also been reported to have structural stability under acid conditions, such as the Ru-N-C system[24]. Therefore, the insightful understanding of how catalytic activity and degradation of the MN_x site related to its electronic structures and local atomic configuration is critical for designing M-N-C catalyst.

Advance in computing capability helps to expand predictions from first-principles simulations of materials. While the materials screening for ORR to date has focused on the electrocatalytic activity[25–27], stability under working conditions is also an essential criterion[28–31]. The demetallation of the metal atom center due to proton attack has been calculated and used to determine the acid stability of the M-N-C catalyst, identifying a specific potential or pH when the dissolution of the metal center is thermodynamically favorable.[32–34] Also, the embedding energy, indicating the bonding strength between embedded isolate metal atom with N-doped carbon structure against the cohesion energy of the bulk metal, is often calculated and used to represent thermodynamic stability for the M-N-C cattalyts[27,33,35]. Previous work on the thermodynamic dissolution of the FeN_4 structures on two different local carbon structures toward aqueous Fe^{+2} has been studied by Glibin et al.[36], suggesting acid stability of the FeN_4 site[36]. In contrast, Holby et al. found FeN_4 sites to be stable only when OH is adsorbed on the FeN_4 site, and the absolute thermodynamic stability of FeN_4 sites remains controversial[37,38].

Various degradation mechanisms of the M-N-C catalyst have been suggested. The carbon oxidation is most probably from H_2O_2-derived radicals during the oxygen reduction, which leads to various oxygen functional groups on the carbon surface that can deactivate the metal site[7] and trigger irreversible leaching of the metal site[19,39]. This might, however, depend on the morphology of the carbon surface[19,39]. However, the carbon surface oxidation is reversible, and the ORR activity can be recovered by electrochemical cycling or chemical treatment[7,22]. Additionally, carbon corrosion can occur and leads to carbon loss surrounding the FeN_x site, eventually resulting in metal site leaching[10]. The demetallation itself has also been proposed to cause fast activity decay of the Fe-N-C catalyst[16]. Thus, the degradation of M-N-C catalysts may have more than

one cause. Nonetheless, how the M-N-C structure affects the stability against demetallation can be the first step to understand the M-N-C degradation, and it is a focus in this work. The relation between the structure and demetallation will be addressed before introducing other possible degradation pathways.

The thermodynamic understanding of dissolution in aqueous media can be obtained from the so-called Pourbaix diagrams, which indicates the potential and pH ranges where the different component oxidation state of materials exist[29,30,40]. A recent study by Holby et al. has proposed a dissolution reaction to determine the stability of FeN_4 embedded on a graphene layer as a function of pH and applied potential[38], indicating the acid instability and likelihood to dissolve of the FeN_4 site. Here, we employ this proposed dissolution to further study the stability of MN_x with various local atomic structures and various metal atoms to understand how local atomic structures and different metal atoms affect the stability of M-N-C catalysts. Furthermore, the acid stability descriptor of the MN_x site under PEMFC conditions is determined by computing the relative stability with respect to the most stable species in the stability diagram, and it is used as a comparative stability descriptor. Thus, the stability descriptor can offer insight into how the M-N-C structure affects stability. The stability descriptor is then used along with the catalytic activity descriptor to identify promising acid-stable and active MN_x sites toward ORR.

2. Methods

2.1 Computation details

Spin-polarized density functional theory calculations are performed using the Vienna ab initio simulation package (VASP)[41] and project augmented wave (PAW)[42] pseudopotential. Structures are set up and analyzed using the atomic simulation environment (ASE)[43]. The exchange and correlation energy are described using the BEEF-vdW functional to include the effects of dispersive interactions[44]. A plane-wave cutoff of 600 eV is used. The self-consistent electron density loop is converged to 10^{-5} eV, and the structures are relaxed until all forces are below 0.025 eV Å^{-1}. The calculations are submitted, managed, and received using the MyQueue[45] workflow tool, a python front-end to the job scheduler.
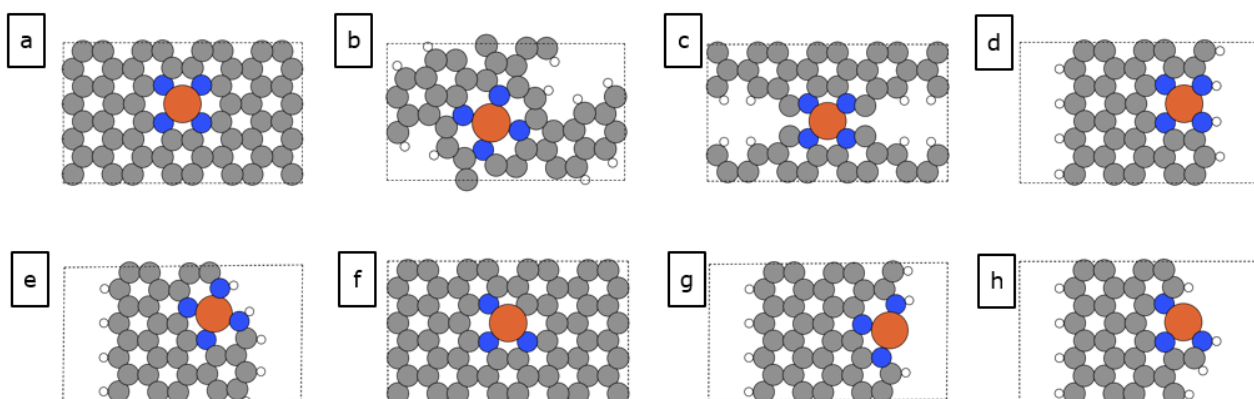
Figure 1: M-N-C model structures: (a) MN_4C_{10}, (b) MN_4C_{12}, (c) MN_4C_8, (d) MN_4C_Z, (e) MN_4C_A, (f) MN_3C_{10}, (g) FeN_3C_Z, (h) FeN_3C_A. Color codes for atom: C-grey, N-blue, H-white, M(= metal atom)-orange.

Eight different M-N-C model structures with different local atomic structure surrounding the metal site are investigated in this study and shown in Figure 1. The MN_4C_{10} structure is an MN_4 site embedded in an intact graphitic layer where the MN_4 site is surrounded by 10 carbon atoms, where M is a single metal atom. The MN_4C_Z and MN_4C_A structure represent the MN_4 site near the zigzag and armchair graphitic edge, respectively. For the active sites hosted in a micropore, we consider a MN_4C_{12} site near the micropore with a porphyrin-like structure and a MN_4C_8 site where the MN_4 moiety is bridging two adjacent armchair edges. The FeN_4C_{12} site has been identified by x-ray absorption spectroscopy and has been proposed as the active site toward the ORR reaction by Zitolo et al.[13]. The FeN_4C_8 site has been proposed as the most active site in such Fe-N-C catalyst[14,15,18,46]. Li et al. have reported that the Fe-N-C catalyst initially comprises two distinct FeN_4 sites identified as the FeN_4C_{10} and FeN_4C_{12} strcuture[19]. Also, we further consider two defective sites derived from the MN_4C_Z and MN_4C_A structure, namely MN_3C_Z and MN_3C_A. These edge-anchored unsaturated MN_3 structures are possible to form under a synthesis environment, as reported by Cheng et al.[47]. The unit cell dimensions in the catalyst plane are 16.9 x 9.8 Å on average, with minor variations for the different metal atoms M (where M = Cr, Mn, Fe, Co, Ni, and Ru) and different local atomic structures. The vacuum layer in a perpendicular direction to the catalyst plane is about 15 Å, and a dipole correction is used in the perpendicular direction to the catalyst plane to decouple the electrostatic potentials on the two sides of the catalyst plane. The Brillouin zone is sampled with a (3×3×1) MonkhorstPack k-point mesh[48].

Solvent effects on the surface and adsorbates are included using the implicit solvent model implemented in VASPsol with a dielectric constant of 80[49,50] representing water medium. Additional calculations with an explicit solvation effect are performed with one explicit water layer. First, the explicit water layer structure (16 H_2O molecules) and the explicit water layer with ORR intermediate structure (15 H_2O molecules surrounding an intermediate) on the FeN_4C_{10} structure are determined by the minima hopping algorithm implemented in ASE[51–53]. The minima hopping algorithm is performed to find at least about 30 local minima with the convergence criterion of maximum force on each atom less than 0.05 eV $Å^{-1}$. Next, the lowest energy local minima structure and the local minima structure within 0.1 eV of the lowest structure are relaxed further with maximum force on each atom less than 0.025 eV $Å^{-1}$. Then, the water layer structure with the lowest energy is used in the calculations for the FeN_4C_{10} and other Fe-N-C structures.

The change in reaction free energy with an applied potential, U, and pH was calculated using the computational hydrogen electrode (CHE)[1,54], the free energy of the reaction at a potential of U versus the reversible hydrogen electrode (SHE), and pH is given by.

$$\Delta G(U, pH) = \Delta G(U=0, pH=0) - neU + nk_BTpHln(10) \qquad (1)$$

where n is the number of electrons involved in the reaction, e is the numerical charge of an electron, and k_B is the Boltzmann constant.

$$\Delta G(U=0, pH=0) = \Delta E_{DFT} + \Delta E_{ZPE} + \Delta U_{vib}(T) - T\Delta S_{vib}(T) \qquad (2)$$

where $\Delta G(U=0, pH=0)$ is calculated from DFT and includes the change in electronic energy (ΔE_{DFT}), zero-point energy (ΔE_{ZPE}), vibration energy ($\Delta U_{vib}(T)$) and entropy ($\Delta S_{vib}(T)$) at T = 298.15K. In the case of adsorbates on the catalyst surface, only the vibration frequencies of adsorbate are considered, and the free energy is calculated following the quantum mechanical harmonic approximation.

The energy of O_2 in the gas phase is poorly described by DFT calculations[44]; thus, it is corrected to reproduce experimental free energy of liquid water formation ($2H_2 + O_2 \rightarrow 2H_2O$; ΔG_{H2O} = -4.92 eV). Furthermore, according to the Christensen scheme[55,56], the error in the energy levels of the ORR intermediates specific to the BEEF-vdW functional are corrected as follows

$$\Delta E(O\text{-}O) = 0.20 \text{ eV} \qquad (3)$$
$$\Delta E(H_2O) = -0.03 \text{ eV} \qquad (4)$$
$$\Delta E(H_2) = 0.09 \text{ eV} \qquad (5)$$

2.2   Stability Calculations

Following previous work on a dissolution reaction for FeN_4 site on bilayer graphene-host structure (which is similar to the FeN_4C_{10} structure defined in this study) by Holby et al.[38]. During the dissolution, the Fe metal atom can leave the FeN_4 site on the carbon host structure (FeN_4C) and becomes an aqueous Fe ion, $Fe^{x+}_{(aq)}$ with a charge x, given the resulting metal-dissolved carbon host cavity with various possible degrees of protonation under the acid environment of the dangling bond, N_4CH_n as a product where n is the number of protons bonded with the carbon host cavity. It has been reported that the FeN_4 site embedded in graphene without ligands or ORR intermediates is unstable in acid conditions, whereas the adsorption of OH on FeN_4 makes the FeN_4 site thermodynamically stable[38].

In this work, we employ the above dissolution mechanism to further investigate the stability trend of the M-N-C systems with different local atomic structures surrounding the metal site, as shown in Figure 1 and different metal atoms. The free energy of MN_yC, $*OH\text{-}MN_yC$, and $*O\text{-}MN_yC$ phase relative to dissolved species as a function of potential U and pH are defined by using H_2O in a liquid phase and H_2 in a gas phase as a reference to avoid O_2 calculation and can be written as Equation (7-9). Note that y is the number of N atoms ligating the metal atom. The MN_yC denotes the bare metal site structure, while the $*OH\text{-}MN_yC$ and $*O\text{-}MN_yC$ denote one $*OH$

and *O adsorbate bond with the metal site, respectively. It is assumed that the catalyst surface is in equilibrium with protons, electrons, and liquid water at T=298.15 K, such that oxygen and hydroxyl may be exchanged between the surface and a reference electrolyte through Equation (6)[29].

$$MN_yC + H_2O(l) \rightleftarrows *OH\text{-}MN_yC + (H^+_{(aq)} + e^-) \rightleftarrows *O\text{-}MN_yC + 2(H^+_{(aq)} + e^-) \qquad (6)$$
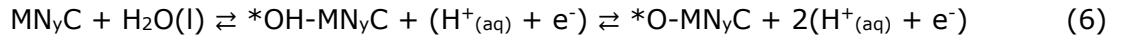
$$MN_yC + nH^+_{(aq)} \rightarrow M^{x+}_{(aq)} + N_yCH_n + (x\text{-}n)e^-$$

$$\Delta G(MN_yC) = G(M^{x+}_{(aq)}) + G(N_yCH_n) - G(MN_yC) - \frac{n}{2}G(H_2) - (x\text{-}n)U + nk_BTln(10)pH \qquad (7)$$

$$*OH\text{-}MN_yC + (n+1)H^+_{(aq)} \rightarrow M^{x+}_{(aq)} + N_yCH_n + (x\text{-}n\text{-}1)e^- + H_2O$$

$$\Delta G(*OH\text{-}MN_yC) = G(M^{x+}_{(aq)}) + G(N_yCH_n) + G(H_2O) - G(MN_yC) - \frac{(n-1)}{2}G(H_2) - (x\text{-}n\text{-}1)U + (n\text{-}1)k_BTln(10)pH \qquad (8)$$

$$*O\text{-}MN_yC + (n+2)H^+_{(aq)} \rightarrow M^{x+}_{(aq)} + N_yCH_n + (x\text{-}n\text{-}2)e^- + H_2O$$

$$\Delta G(*OH\text{-}MN_yC) = G(M^{x+}_{(aq)}) + G(N_yCH_n) + G(H_2O) - G(MN_yC) - \frac{(n-2)}{2}G(H_2) - (x\text{-}n\text{-}2)U + (n\text{-}2)k_BTln(10)pH \qquad (9)$$

where $\Delta G(MN_yC)$, $\Delta G(*OH\text{-}MN_yC)$, $\Delta G(*O\text{-}MN_yC)$ are the free energy of the catalyst surface without and with one *OH, and one *O at the metal site, respectively. $\Delta G(N_yCH_n)$ is the free energy of the metal-dissolved carbon cavity with n H atoms bonded at the cavity. We consider from n=0 up to n=4 for the dissolution reaction in Equation (7-9). The optimized structures of nH-bond carbon cavity are shown in Figure S1. $G(M^{+x})$ is the free energy of the dissolved metal ion, is estimated as follows:

$$G(M^{+x}) = E_{DFT(bulk)} + \Delta G_x \qquad (10)$$

where $E_{DFT(bulk)}$ is the total energy per metal atom in the bulk structure obtained from DFT calculations. ΔG_x is the free reaction energy of the dissolution reaction of the bulk metal, which is taken from the literature[57–59]. Table S1 shows the free energy of the dissolved metal ion and the dissolution potential used in each approximation ΔG_x. The free energy of the dissolved ion depends on the metal ion concentration, which is assumed to be 10^{-6} M for all dissolved metal ions in this work and all calculations are at T=298.15 K.

2.3 ORR catalyst activity

We employ purely thermodynamic models when considering the ORR activity by assuming that all element steps have to be exergonic for the ORR to run and neglect the kinetic barrier for each elementary step. The ORR catalytic activity of the different surface structures is estimated

by determining the theoretical overpotential and the potential-determining step in the four-electron associative mechanism with *O, *OH, and *OOH intermediates[60] as shown in Equation (11-14). The metal site is considered as the active site, so all ORR intermediates bond with the metal site. The potential and pH dependence of each reaction step is calculated by employing the CHE as shown in Equation (1).

$$O_2(g) + H^+ + e^- + * \rightarrow *OOH \qquad ; \Delta G_1 \qquad (11)$$

$$*OOH + H^+ + e^- \rightarrow *O + H_2O(l) \qquad ; \Delta G_2 \qquad (12)$$

$$*O + H^+ + e^- + * \rightarrow *OH \qquad ; \Delta G_3 \qquad (13)$$

$$*OH + H^+ + e^- \rightarrow * + H_2O(l) \qquad ; \Delta G_4 \qquad (14)$$
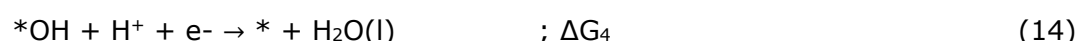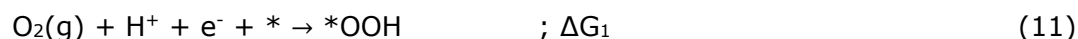
where * denotes the active metal site. The limiting potential (U_L) is defined as the highest potential at which all four reaction steps are downhill in free energy.

$$\text{Overpotential} = 1.23 \text{ V} - U_L = 1.23 \text{ V} - \max\{\Delta G_1, \Delta G_2, \Delta G_3, \Delta G_4\} / e \qquad (15)$$

Adsorption energies of *O, *OH, and *OOH intermediate are defined relative to a water molecule from the following reactions.

$$* + H_2O \rightarrow *O + H_2 \quad ; \Delta G(*O) \qquad (16)$$

$$* + H_2O \rightarrow *OH + \frac{1}{2}H_2 \qquad ; \Delta G(*OH) \qquad (17)$$

$$* + 2H_2O \rightarrow *OOH + \frac{3}{2}H_2 \qquad ; \Delta G(*OOH) \qquad (18)$$

3 Results and Discussion

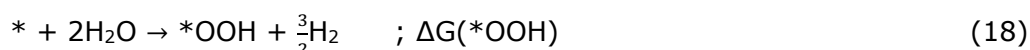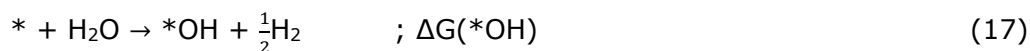### 3.1 Stability diagram and thermodynamic driving force toward metal dissolution.

We first consider the Fe-N-C system. Figure 2 shows the stability diagram of the FeN_4C_{10}, FeN_4C_{12}, and FeN_4C_8 structures as a function of applied potential, U, and pH. The stability diagrams for other FeN_yC structures are shown in Figure S2. At acidic ORR relevant conditions (U ~ 0.6-0.8 V_{SHE} and pH = 0), the most stable phase is the dissolved Fe ions for all considered structures, so the single Fe metal atom is prone to leach. At the same potential range in alkaline conditions, *OH or *O can be formed from water on the Fe metal site on the FeN_4C_{10}, FeN_4C_{12}, FeN_4C_A, FeN_4C_Z, and FeN_3C_{10} structure results in stabilizing the Fe metal site against the dissolution. However, the FeN_4C_8, FeN_3C_Z, and FeN_3C_A structures are still prone to dissolution even in alkaline conditions, as the most stable phase is still a dissolved Fe compound ion. In general, the calculation reveals that the dissolution is a greater problem in acidic than alkaline conditions, as reported by previous experiments[12,61].

To further extend the stability diagram, we consider a thermodynamic driving force toward the dissolution. A previous study by Singh et al. suggests that materials with predicted free energy

up to 0.5 eV/atom greater than the most stable species in the Pourbaix diagram can be stable against the corrosion in experiments due to a large kinetic barrier for structural reorganization[40]. We define the relative dissolution free energy (ΔG_R), which is the free energy difference between the most stable Fe, *OH-Fe, or *O-Fe phase, and the most stable dissolved species at pH = 0. The ΔG_R represents a thermodynamic driving force for each phase toward the dissolution and is shown in Figure 2(d-f), where the most stable dissolved species are superimposed as horizontal bars at the bottom. The phase with a higher driving force is likely to dissolve into the electrolyte, as reported by the previously combined experimental and theoretical study[30].

For the considered FeN_yC structures, the relative dissolution free energy (ΔG_R) value of the bare Fe metal phase order at U = 0.8 V_{SHE} and pH = 0 is FeN_4C_A < FeN_4C_Z < FeN_4C_{10} < FeN_3C_{10} < FeN_4C_{12} < FeN_3C_Z < FeN_4C_8 < FeN_3C_A, see Figure 2(g), suggesting that the stability against the dissolution decreases from FeN_4C_A to FeN_3C_A. The formation of one *OH and *O on the bare Fe metal site at higher potential thermodynamically stabilizes the Fe metal atom against the dissolution. At U = 0.8 V_{SHE} and pH =0, the relative free energy (ΔG_R) order of the most stable phase is found to be *O-FeN_4C_A < *O-FeN_4C_Z < *O-FeN_4C_{10} < *OH-FeN_3C_{10} < *O-FeN_4C_{12} < *O-FeN_3C_Z < *O-FeN_3C_A < *OH-FeN_4C_8, see Figure 2(g).

At potentials in the range 0.2-0.9 V_{SHE} and pH = 0; we find that the FeN_4C_{10} Structure is more stable than the FeN_4C_{12} site as the thermodynamic driving force for the most stable phase of the FeN_4C_{12} structure is about 0.70 eV greater than that of the FeN_4C_{10} structure, on average. These results agree with the experimental results reported by Li et al.[19]

The horizontal bars at the bottom of each relative stability plot indicate the most energetically favorable dissolved species, suggesting that the dissolution reactions depend not only on the working condition (U and pH) but also on the local atomic structure around the metal site. For example, for the FeN_4C_8, FeN_4C_A, and FeN_4C_Z structures, the dissolution reaction results in 0 or one proton transferred to the cavity site, while 1-3 protons are transferred to the cavity site of the other structures.
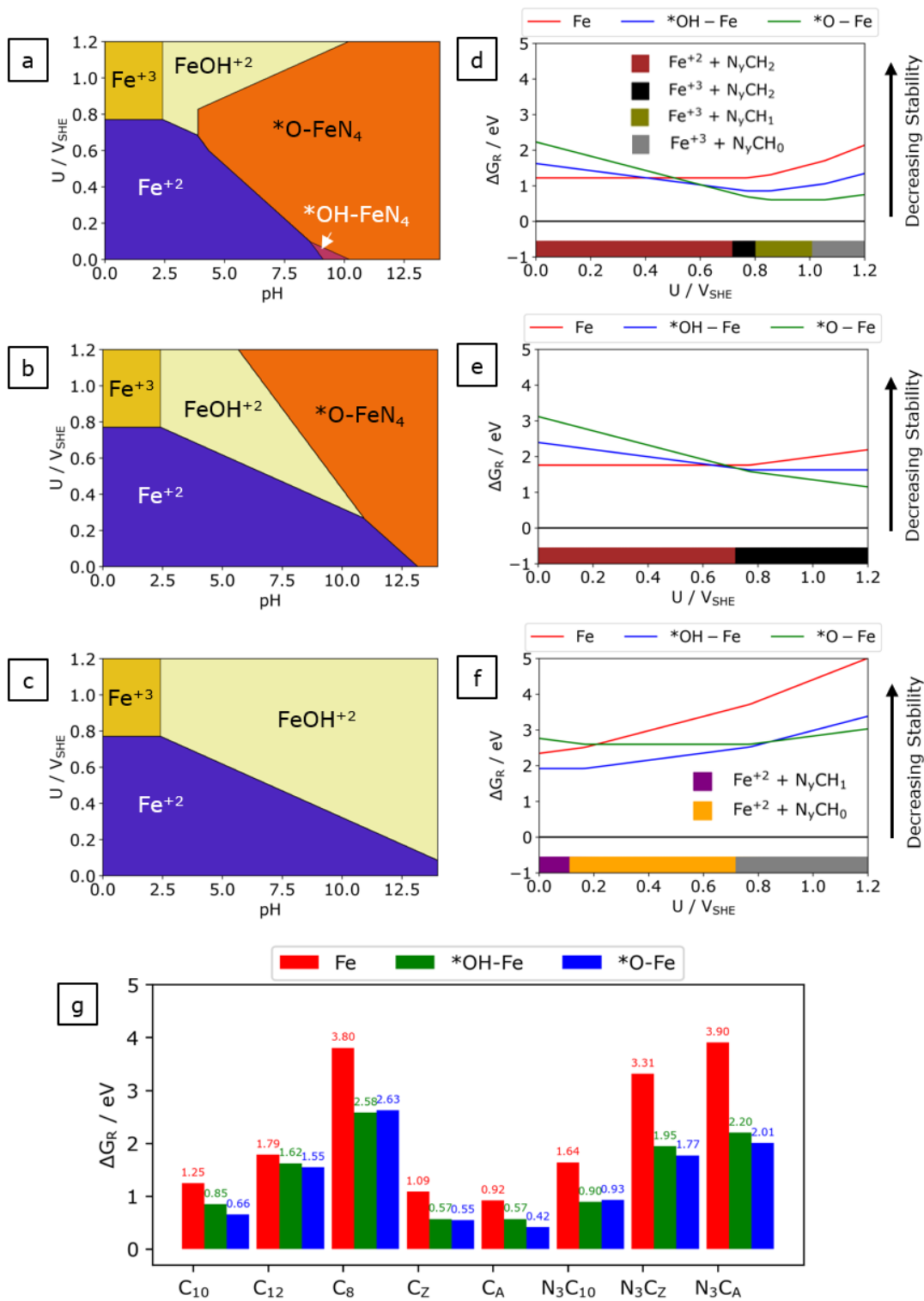
Figure 2: (a-c) Stability diagram of FeN$_4$C$_{10}$, FeN$_4$C$_{12}$, and FeN$_4$C$_8$ structure as a function of applied potential (U) and pH. (d-f) The relative stability (ΔG_R) for Fe, *OH-Fe, and *O-Fe phase as a function of potential U at pH = 0 for FeN$_4$C$_{10}$, FeN$_4$C$_{12}$, and FeN$_4$C$_8$ structure, the most energetically favorable dissolved species are superimposed as horizontal bars at the bottom of each relative stability plot. (g) Relative stability for Fe, *OH-Fe, and *O-Fe phase of different considered FeN$_y$C structures in Figure 1 at U = 0.8 V$_{SHE}$ and pH = 0.
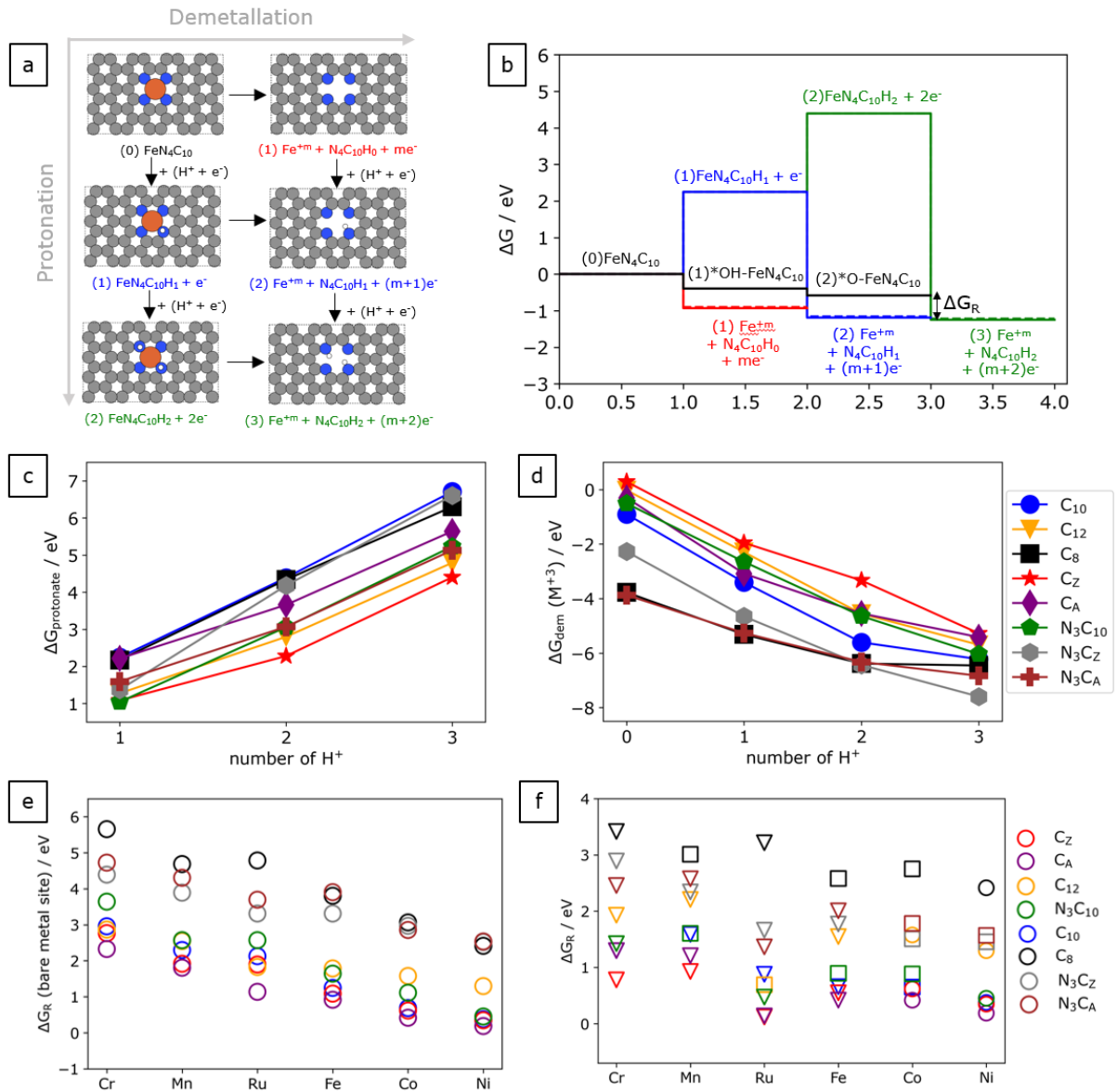
Figure 3: (a) Schematic illustration of possible dissolution mechanism of FeN_4C_{10} structure. Color codes for atoms are the same as Figure 1. (b) Free energy diagram related to possible dissolution mechanisms of FeN_4C_{10} structure with up to $3H^+$ at $U = 0.8$ V_{SHE} and pH = 0. (c) Protonation free reaction energy ($\Delta G_{protonate}$) at the atoms surrounding the Fe metal site and (d) demetallation free reaction energy (ΔG_{dem}) for Fe metal atom from the considered host carbon structures to dissolved Fe^{+3} ion as a function of H^+ number at pH = 0 and $U = 0.8$ V_{SHE}. (e) The relative stability (ΔG_R) of the bare metal phase and (f) the most stable phase MN_yC structures at $U = 0.8$ V_{SHE} and pH = 0. The symbols for the surface: *M=circle, *OH-M=square, *O-M=triangle.

Considering the dissolution reaction in more detail, we find that the protonation at the metal-dissolved host carbon structure is thermodynamically favorable for the N_4C_{12}, N_3C_{10}, N_4C_Z, N_4C_A, N_4C_{10}, and N_3C_Z structure, but it is endothermic for the N_3C_A and N_4C_8 structure (Figure S3). However, these proton transfers might not necessarily affect the kinetic dissolution rate if they occur late in the exothermic process. During the dissolution, we therefore also consider that the protonation reaction occurs at the atoms surrounding the Fe metal atom and is followed by the demetallation reaction, as Equation (19-20). Figure 3(a-b) illustrates the possible dissolution mechanism and corresponding free energy diagram of the dissolution process. From a thermodynamic perspective, whether the protonation reaction occurs before or after the demetallation leads to the same overall dissolution reaction as Equation (7) and the same relative stability.

$$FeN_yC + n(H^+ + e^-) \rightarrow FeN_yCH_n \tag{19}$$

$$FeN_yCH_n \rightarrow Fe^{+m} + N_yCH_n + me^- \tag{20}$$
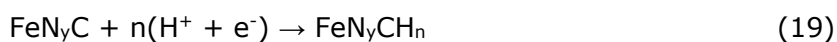
We find that the protonation at the atoms surrounding the Fe metal atom is endothermic and becomes more difficult as the potential increases or more protons are added (Figure 3(c)). At the potential $U = 0.8$ V_{SHE} and pH =0, the order of the protonation (from easy to difficult) is FeN_4C_Z > FeN_4C_{12} ~ FeN_3C_{10} ~ FeN_3C_A > FeN_3C_Z ~ FeN_4C_A > FeN_4C_{10} > FeN_4C_8. On the other hand, the demetallation reaction becomes more favorable after the atoms surrounding the Fe metal atoms are protonated and become more favorable as potential increases or more protons are added (Figure 3(d)). The order of the demetallation at $U = 0.8$ V_{SHE} and pH = 0 (from easy to difficult), regardless number of additional protons before the demetallation is FeN_4C_8 ~ FeN_3C_A > FeN_3C_Z > FeN_4C_{10} > FeN_4C_A ~ FeN_3C_{10} ~ FeN_4C_{12} > FeN_4C_Z. Additionally, we find that the Fe metal atom in the FeN_4C_8, FeN_3C_Z, and FeN_3C_A structure bond quite weakly with the host carbon structure compared to the others, as reported by Tan et al.[39]. Therefore, the Fe metal atom in these structures can more easily leave the host carbon structure.

The demetallation reaction relates to the bond strength between the Fe metal atom and the host carbon structure. The protonation at the ligand atoms surrounding the Fe metal atom can weaken the bond between the Fe and the surrounding ligand atoms, resulting in the following demetallation step being facile. Consequently, the basicity of ligand atoms contributes to the stability of the Fe-N-C catalyst in the acidic condtion[12,20] as same as the bonding strength between the metal atom with the carbon host structure. The different trade-offs between the demetallation reaction and the protonation reaction due to the different local atomic structures surrounding the Fe metal site enable different n values for the dissolution reaction.

It is important to note that the real degradation mechanism is still unknown, and other possible mechanisms such as carbon corrosion[10,18], hydroxyl radical attraction[6,62], and carbon oxidation[7] have been proposed as a degradation mechanism of the Fe-N-C catalyst can

simultaneously occur and might be coupled. Also, the stability is here analyzed from thermodynamic trends, whereas the rate of metal leaching is determined by the kinetic activation energy. Thus, a kinetic analysis of the dissolution mechanism would be required for a complete theoretical description.

Furthermore, Holby et al. suggest the computational unit cell size and a graphene underlayer to host the FeN_4 actives site influence the calculated stability[38]. To assess the sensitivity to these choices, we performed additional stability calculations for some Fe-N-C structures with a bigger unit cell (Figure S5). Table S4 shows the dissolution potential to Fe^{+2} ion obtained from two sizes of a unit cell. The size of the unit cell can lead to variation in the dissolution potential of about 0.08 V_{SHE}. However, we find the same trend in the dissolution potential obtained from both sizes of unit cells which is FeN_4C_8 (-1.09 V_{SHE}) < FeN_4C_{10} (0.35 V_{SHE}) < FeN_4C_A (0.65 V_{SHE}) < FeN_4C_{12} (0.79 V_{SHE}) < FeN_4C_Z (0.94 V_{SHE}) for the unit cell in Figure 1 and FeN_4C_{8b} (-0.98 V_{SHE}) < FeN_4C_{10b} (0.27 V_{SHE}) < FeN_4C_{Ab} (0.52 V_{SHE}) < FeN_4C_{12b} (0.73 V_{SHE}) < FeN_4C_{Zb} (0.97 V_{SHE}) for the bigger unit cell in Figure S5. This dissolution trend agrees with the trend reported by Tan et al.[39]. However, we find the dissolution to Fe^{+2} ion of 0.35 V_{SHE} and 0.27 V_{SHE} for the FeN_4C_{10} and FeN_4C_{10b} structure, respectively, which are quite different from the value reported by Holby et al. using the FeN_4C_{10} Structure on a 6x6 graphene monolayer structure in a vacuum in which the dissolution potential is 0.57 V_{SHE}. We find that the dissolution potential of 0.47 V_{SHE} for the FeN_4C_{10} Structure (Table S5) in a vacuum. Thus, there may be some influence of solvation on the calculated stability as well as the strain associated with the smaller cell[38]. The variation in *O and *OH free adsorption energy due to the size of the unit cell is 0.08 and 0.07 eV on average for both *O and *OH, respectively. The trend in the relative dissolution free energy (ΔG_R) value of the most stable phase at U = 0.8 V_{SHE} and pH = 0 obtained from the bigger unit cell is: *O-FeN_4C_{Ab} < *O-FeN_4C_{Zb} < *O-FeN_4C_{10b} < *O-FeN_4C_{12b} < *OH-FeN_4C_{8b}, in agreement with results on the unit cell in Figure 1. Therefore, the unit cells in Figure 1 are used in our further calculations.

Besides the stabilization by the graphene underlayer reported by Holby et al., the dissolution potential of 0.65 V_{SHE} has been reported for the FeN_4C_{10} configuration on a 6x6 graphene bilayer structure (0.08 higher than the monolayer structure)[38]. Thus, it has been recommended to use a larger and bilayer graphene structure for the stability calculation[38]. However, we find that different local atomic structures around the Fe metal site cause the change in the dissolution potential in the range of 0.30 - 1.43 V_{SHE} which is greater than the effect of a graphene underlayer. Thus, only a monolayer structure is considered here.

So far, the solvent effect is considered implicitly in this work. We further investigate the effect of the explicit water layer on the stability calculation. We consider the explicit water layer only on the same side of the catalyst as the *O and *OH adsorbates (Figure S6). A previous study by Svane et al. [63] studied the explicit solvation effect on a CoN_4C_{12} structure suggests that the explicit water on the same side of the adsorbate can result in stabilization about 0.27 eV for *OH relative to a solvent-free model. However, no further stabilization effect when adding explicit water layers

on both sides of the catalyst surface as the stabilization is only about 0.1 eV for *O, *OH, and *OOH relative to the one explicit water on the same side with the adsorbates. Table S5 shows the dissolution potential to Fe^{+2} obtained from different solvation models. The dissolution potentials obtained from implicit solvation are 0.14 V_{SHE} lower, on average than those obtained in a vacuum. The dissolution potential with the explicit solvation is close to those in a vacuum with a variation of 0.06 V_{SHE}, on average. However, there is a big difference in dissolution potential between FeN_4C_z in a vacuum and explicit solvation. We find that, in the optimized structure of the $N_4C_{zw}H_0$ structure with one explicit water layer, the nitrogen atoms are out of a carbon plane while the nitrogen atoms in a vacuum and implicit solvation model remain in the carbon plane. The distortion with the explicit solvation leads to 0.20 V_{SHE} lower dissolution potential for the FeN_4C_{zw} compared to the solvation-free model. The explicit water layer surrounding *O and *OH adsorbates leads to stabilization relative to the vacuum of 0.41 and 0.22 eV, respectively. The stabilization relative to the vacuum due to the implicit solvation is 0.30 and 0.22 eV for *O and *OH, respectively. Thus, the stabilization is similar in magnitude for implicit and explicit solvation. For the most stable phase at U = 0.8 V_{SHE} and pH = 0, the relative dissolution free energy (ΔG_R) value with explicit solvation is *O-FeN4C10$_{zw}$ < *O-FeN4C10$_w$ < *O-FeN4C12$_w$ < *O-FeN4C8$_w$. Meanwhile, we find the relative dissolution free energy (ΔG_R) value in vacuum to be: *OH-FeN4C10$_{zv}$ < *OH-FeN4C10$_v$ < *OH-FeN4C12$_v$ < *OH-FeN4C8$_v$. The difference in the relative stability of the most stable phase is mainly due to the different stabilization effects on *O and *OH via different solvation models. There is an obvious influence of solvation on the stability calculation; to avoid the structural distortion in the calculations, we use the implicit solvation, which leads to a similar solvation stabilization as the explicit solvation in our further calculations.

We further extend the thermodynamic stability analysis with different metal atoms, changing the metal atom to Cr, Mn, Co, Ni, and Ru. The stability diagrams are shown in Figure S10-S15, indicating that all considered MN_x sites on the considered structures prefer to dissolve under the acid condition as the most stable species at pH = 0 are an aqueous metal ion. Figure 3(e) shows the relative stability for the bare metal site at U = 0.8 V_{SHE} and pH = 0; the MN_4C_8, MN_3C_z, and MN_3C_A structures, regardless of the metal atom, are less stable than other structures. On the other hand, the MN_4C_A structure is the most stable structure against the dissolution under the same acid conditions, regardless of the metal atoms. The general trend in the thermodynamic driving force toward the dissolution of the bare metal site at U = 0.8 V_{SHE} and pH = 0 is Cr > Mn > Ru > Fe > Co > Ni. To understand this trend, we have considered the dissolution of the bare MN_x site without the protonation at the cavity. We first consider the energy of the metal atom being in the MN_x site on the carbon host structure against the formation of metal atom in the bulk structure by the following Equation:

$$\Delta G_{bulk} = E_M + E\left(N_x C_y\right) - E(MN_x C_y) \tag{21}$$

where E_M is the total energy per atom of the metal in bulk structure, $E(MN_xC_y)$ is the total energy of the MN4 structure and $E(N_xC_y)$ is the total energy of the metal-dissolved cavity structure (N_xC_y). The calculated ΔE_{metal} for different metal centers on different carbon host structures are shown in Figure S16(a) and Table S6. The ΔE_{metal} values indicate that the metal atom in the MN4C8, MN3CZ, and MN3CA structure is unstable and prefers to form the bulk metal rather than embedded in the carbon host structure compared to other structures. Secondly, we consider the energy for oxidizing the metal atom at a working potential (U=0.8 VSHE) by the following Equation:

$$\Delta E_{oxidize} = G(M^{+x}) - xU - E_M \tag{22}$$

where $G(M^{+x})$ is free energy of the most stable dissoved metal ion at the considered condition (x=2 for M=Co and Ni; x = 3 for M=Cr, Mn, Ru and Fe). The calculated $\Delta E_{oxidize}$ is shown in Figure S16(b) and Table S6. The oxidization trend of the metal (from easy to difficult) is Cr < Mn < Fe < Co < Ni. For these 3d metals, the metal oxidation energy ($\Delta E_{oxidize}$) play an important role in the dissolution reaction, causing a significant difference in the acid stability among 3d elements. The stability of the bare MN_x site toward a dissolved metal cation is Cr < Mn < Fe < Co < Ni, following the oxidation trend.

For Ru, the bond strength between the Ru atom and the carbon hosts is weaker than other metal elements within the same carbon host structure. However, Ru is also more difficult to oxidize, and overall, the stability of the RuN_x site is between Mn and Fe.

The formation of one *O and *OH from water mostly on Cr, Mn, Ru, and Fe metal sites at pH = 0 and U = 0.8 VSHE is thermodynamically favorable on most of the considered structures, resulting in increased stability under acid conditions. However, under the same conditions, the most stable phase of the considered CoN_yC and NiN_yC structures is mostly the bare metal site (Figure 3(f)).

We consider the M-N-C catalyst by choosing M = Cr, Mn, Fe, Ru, Co, and Ni because these elements are either relatively cheap and abundant 3d metals or have shown promising ORR activity and stability. The thermodynamic stability analysis of the Pt-N-C structures is also considered and shown in Figure S17. Most of the considered Pt-N-C structures, except PtN4C8, are thermodynamically stable against dissolution at pH = 0, U = 0.8 VRHE, and even more stable than other considered metal elements. However, all considered Pt-N-C structures are inactive toward the ORR as the overpotential of all considered Pt-N-C structures is more than 1.00 eV (Table S18).

In general, we find that the metal atom on the graphene plane (MN4C10 or MN3C10) and the MN4 site on the graphene edge (MN4CZ and MN4CA) are more stable than the MN4 site hosted near micropores (MN4C12) or bridging between two zigzag edges (MN4C8) and the MN3 structures at the graphene edge (MN3CZ and MN3CA).

The Fe, Co, Ru, and Ni metal atoms on the MN_4C_{10}, MN_4C_Z, and MN_4C_A can well be kinetically stable under acid conditions as the thermodynamic driving force is less than 0.70 eV at U = 0.8 V_{SHE} and pH = 0. On top of that, the Ru metal atom on the MN_4C_Z, MN_4C_A structure, and Ni metal atom on the MN_4C_A structure are the most promising stable structure under the acid condition as the thermodynamic driving force toward the dissolution is less than 0.2 eV. Previous experimental results have found that the Ru-N-C catalyst is rather stable in the acid environment with a dissolution rate of less than 5% over 30-hour of operation at 1.5 V_{SHE}[24]. Meanwhile, the Cr and Mn metal atoms on considered structures have a considerable driving force toward dissolution (>0.7 eV), so these catalysts are unstable during the PEMFC operation. A previous experimental study has reported that the Mn-N-C catalyst is likely to lose its ORR catalytic activity more than the Fe-N-C catalyst in acid and alkaline conditions during the stability test cycling the potential between 0.5 and 1.3 V_{SHE}[61]. Furthermore, the previous experiments have suggested that the Co-N-C catalyst has significantly enhanced resistance to demetallation compared to the Fe-N-C catalyst in acid conditions, especially under O_2 purged testing[22]. For the FeN_yC and CoN_yC structure without any adsorbate, the thermodynamic driving force of the bare Fe metal atom toward the dissolution is about 0.56 eV bigger than for the bare Co metal site, on average. With the formation of one *OH or *O on the metal site, the relative stabilities of the most stable phase under acid conditions for both metal atoms are comparable. This suggests that other mechanisms such as carbon surface oxidation[7] as well as the H_2O_2 derived radicals attack stabilized *OH or *O ligand[22,62] possibly occur along with the demetallation reaction or deactivate the active site. These possible processes should be included in the calculation model to get a complete theoretical description.

Different metal atoms on the same carbon structure dissolve with the same dissolution reaction; the same n value in Equation (7-9). With the n=0 dissolution reaction, the primary contribution to acid instability is the bond strength between the single metal atom and the host carbon structure. While with increasing n, more contributions from the protonation reaction at the atom surrounding the metal site are included. Thus, the thermodynamic acid stability of the M-N-C catalyst is determined by both the bonding strength of the metal atom with the host carbon structure and the basicity of the ligand atom around the metal atoms. In the Fe-N-C system, the FeN_4C_{12} has strong bonding between the Fe metal atom and the host carbon structure, but the nitrogen atoms around the Fe metal site are vulnerable to proton attack. The nitrogen ligand in the FeN_4C_8 structure can resist the action of protons in acid solution, but the bonding between the Fe metal atom and the carbon host structure is too weak. Consequently, both structures are predicted to be less stable than the FeN_4C_{10} structure under the same acid conditions.

Additionally, previous studies by Zhang et al.[64] and Jung et al.[65] have suggested that the oxygen functional groups near the CoN_4 site can be formed via electrochemical or chemical treatment. The formation energies of *O from water on various carbon sites near the CoN_4C_{10} structure reported by Zhang et al.[64] and Jung et al.[65] are more than 2.8 eV, suggesting weak

adsorption of *O on the adjacent carbons. The oxidation of the surface carbon adjacent to the FeN$_4$ sites has also been reported, decreasing the four-electron ORR activity. However, the deactivation is reversible, and the ORR activity can be recovered upon electrochemical reduction of the carbon surface[7]. We consider *O or *OH formation on carbon adjacent to the Fe center on the FeN$_4$C$_{10b}$, FeN$_4$C$_{12b}$, and FeN$_4$C$_{Zb}$ structures, assuming that the catalyst surface is in equilibrium with protons, electrons, and liquid water at T=298.15 K (Figure S19). The *O or *OH on adjacent carbon is not thermodynamically favored in the potential range of 0-1.2 V$_{SHE}$. Thus, we exclude the formation of *O and *OH next to the MN$_x$ site from our further considerations.

However, the surface carbon oxidation can possibly occur via other such as the dissociation of H$_2$O$_2$[7] or *OOH[39]. The surface carbon oxidation may directly or indirectly affect the dissolution of the MN$_x$ site[19]. Tan et al. [39] has suggested that the stable oxygen functional group site next to the FeN$_4$ site can be different, depending on the local carbon structure.

We consider the effect of nearby *O and *OH on the dissolution reaction for some specific Fe-N-C structures. The carbon surface oxidation potentially affects the stability of the MN$_x$ site and the dissolution reaction. As shown in Table S8, the bond strength between Fe and carbon host in the FeN$_4$C$_{10}$ structure and bond strength between one H with the carbon cavity in the N$_4$C$_{10}$ structure is strengthened by the nearby *OH functional but weakened by the nearby *O functional. Breaking the Fe-N bonds require more energy with nearby *OH; however, the H binding with the cavity is also more energetically favorable in the final product. Overall, at pH = 0 and U = 0.8 V$_{SHE}$, the pristine FeN$_4$C$_{10}$ with the nearby *OH has the same dissolution (n=1) reaction product as the pristine FeN$_4$C$_{10}$ structure but the dissolution reaction is more thermodynamically favorable than the pristine FeN$_4$C$_{10}$ structure (Figure S20). The thermodynamic driving force towards the dissolution of the pristine FeN$_4$C10$_{bOH}$ is found to be 1.58 eV, 0.37 eV higher than that of the pristine FeN$_4$C$_{10}$. For the FeN$_4$C$_{10}$ with nearby *O functional, the Fe-N and H-N bonding become weak. At pH = 0 and U = 0.8 V$_{SHE}$, the overall dissolution reaction is more thermodynamically favorable to occur via the n=0 reaction for the pristine FeN$_4$C10$_{bO}$, and it is more thermodynamically favorable than the pristine FeN$_4$C$_{10}$ structure. The thermodynamic driving force toward the dissolution for the pristine FeN4C$_{10bO}$ is 1.87 eV, 0.66 eV higher than the pristine FeN$_4$C$_{10}$ structure.

In the cases of the pristine FeN$_4$C$_{12}$, the Fe-N and H-N bond strength are weakened by both the nearby *O and *OH functional groups. The same dissolution (n=2) reaction as the pristine FeN$_4$C$_{10}$ structure becomes more energetically favorable with nearby *O and *OH. The thermodynamic driving force toward the dissolution is 2.01, 1.98 eV for the pristine FeN$_4$C$_{12bOH}$ and FeN$_4$C$_{12bO}$ structure (0.36, 0.33 eV higher than that of the pristine FeN$_4$C$_{12}$).

At the same time, the formation site of these stable oxygen functional groups can depend on the carbon structure around the active site (Table S7). Therefore, the effect of the carbon

surface oxidation on the stability of the MN_x site can vary for different local carbon structures[39]. How carbon surface oxidation forms on various carbon structures and its corresponding effect on the dissolution reaction of the MN_x active site would certainly be interesting to study. However, such an investigation is beyond the scope of the current study.

In addition to the carbon surface oxidation resulting in *O or *OH on the adjacent carbon atoms to the FeN_x site, the carbon surface could possibly contain additional N heteroatoms. The graphitic N atoms surrounding the FeN_x site have been reported to improve ORR activity in both alkaline and acidic electrolyte. It has been reported that the neighboring graphitic nitrogen induces a higher filling degree of d-orbit and decreases on-site magnetic, which can optimize the binding energy of the ORR intermediates[66]. The stability diagrams of some structures with one and two graphitic N atoms are shown in Figure S22. The structures show no distortion due to the added graphitic N atoms (Figure S23). However, the Fe-N bond strength and the 1st H-N bonding strength on the cavity are weakened due to the added graphic N (Table S9). Consequently, the additional graphitic N atoms are likely to destabilize the surface and increase the thermodynamic driving force toward the dissolution. At pH=0, U =0.8 V_{SHE}, the thermodynamic driving force toward dissolution increases 0.09 and 0.26 eV on average for the FeN_4C_{12} structures with one and two graphitic N atoms, respectively. For the FeN_4C_{10} structure, the thermodynamic driving force toward the dissolution at pH=0 and U=0.8 V_{SHE} increase from 1.25 eV to 1.56 and 1.83 eV on average with one and two graphitic N atoms, respectively. Note that only some specific configurations of the graphitic N on the carbon plane are considered here; different configurations could affect the measured activity[66] and stability. However, the exploration of all such configurations is beyond the scope of this work.

The anion-selective adsorption on the active site of the M-N-C catalyst can occur, and it has been previously reported[25,67] that the effect of anions on the Pt and the Fe-N-C catalyst is different. For Pt, the anion in the electrolyte solution can block the active site, decreasing ORR activity. While the M-N-C catalyst is a two-dimensional material, both sides of the catalyst can be exposed to the electrolyte with anions adsorbing on one or both sides of the catalyst. The adsorption of various anions has been reported to be competitive with formation of *O, *OH on the MN_4C_{12} structure (where M = Fe, Cr, Mn, and Co), and can even promote the ORR activity, depending on the metal center as previously reported Svane et al.[25].

3.2   ORR catalytic activity

As previously seen from the thermodynamic stability results, the formation of one *OH and *O adsorbate from water on the metal site is thermodynamic favorable and stabilizes the metal site against the dissolution. Due to the two-dimensional structure of the MN_y motif, when the formation of one *OH or *O adsorbate from water occurs on the metal site, it can become a part of the active metal site where the other side of the metal atom is still available for the ORR intermediates to react. Thus, in this work, we consider that both metal sides can bond with the

adsorbate. At a relevant PEMFC condition, we can identify the most stable adsorbate, which is likely to occupy one of the metal atom sides and become a part of the active metal site, as shown in Figure 3(f).

In general, we find that one *O or *OH adsorbate is absorbed strongly on the metal site in the MN_4C_8, MN_3C_Z, and MN_3C_A structures compared to other MN_yC structures, even in the case of inactive Ni metal atoms. Thus, one *O or *OH mostly becomes a part of the active metal site in these structures, regardless of the metal atom.

Having identified the most stable phase of the considered MN_yC structures, we investigate how the ORR activity was affected by the local atomic structure around the metal atom as well as the presence of *O and *OH adsorbate as a part of the active metal site. The adsorption free energy of the reaction intermediate *OOH, *O, and *OH and the limiting potential for the associative ORR pathway is calculated as defined in the Method section. An initial chemical step of O_2 adsorption is not explicitly considered. Liu et al. [17] reported that the activation energy for the direct O_2 dissociation reaction is always higher for the OOH dissociation reaction on the FeN_4C_{10}, FeN_4C_{12}, and FeN_4C_8 structure; thus, the OOH dissociation path is kinetically more feasible than the O_2 dissociation pathway.

The MN_yC catalyst follows the scaling relation between the adsorption energies of the *OH and *OOH intermediates, which is known for metal and oxide surface[68].

$$\Delta G(*OOH) = \Delta G(*OH) + 3.23, MEA = 0.11 \text{ eV} \qquad \text{Equation (21)}$$

A similar scaling relation obtained from the MN_4 catalyst has been previously reported by Svane et al.[25]. This scaling relationship implies that the best liming potential is 0.83 V_{SHE}, resulting in the minimum overpotential of 0.4 V_{SHE}. The limiting potential plotted as a function of $\Delta G(*OH)$ for each metal atom, and the corresponding ORR overpotential is shown in Figure 4.

We first consider the Fe-N-C system, the bare Fe metal site bond with *OH intermediate quite strongly, so the reaction is limited by the reduction of *OH (Equation (14)) for the considered carbon host structures. The trend in ORR overpotential for the bare Fe metal site is found to be $FeN_4C_{12} < FeN_4C_A < FeN_4C_{10} < FeN_4C_Z < FeN_3C_{10} < FeN_4C_8 < FeN_3C_Z < FeN_3C_A$. This trend agrees with a previous theoretical prediction by Yang et al. [69]. At U = 0.8 V_{SHE} and pH = 0, we find that one side of the Fe atom is likely to be ligated by either *OH or *O adsorbate. The active site with the *O or *OH ligand is denoted as *OH-Fe and *O-Fe in Figure 4. The ORR intermediate bind with the Fe metal site weaklier with the presence of *OH ligand, compared to those on the bare Fe metal site. The ORR intermediate binding becomes even weaker with the presence of the *O ligand. The *OH ligand is found to improve ORR activity on the FeN_4C_{10}, FeN_4C_{12}, FeN_4C_8, FeN_4C_Z, and FeN_3C_{10} structure as reported by previous studies[69–72]. Whereas the *O ligand promotes the ORR activity on the FeN_3C_Z and FeN_3C_A structures. Considering the ORR activity on the most stable phase under the PEMFC relevant condition in Figure 3(f), we find the ORR overpotential trend to

be *OH-FeN$_4$C$_8$ (0.43) < *O-FeN$_3$C$_Z$ (0.54) ~ *OH-FeN$_3$C$_{10}$ (0.56) < *O-FeN$_3$C$_A$ (0.56) < *O-FeN$_4$C$_{10}$ (0.63) < *O-FeN$_4$C$_{12}$ (0.80) < *O-FeN$_4$C$_A$ (0.81) < *O-FeN$_4$C$_Z$ (1.06).

We find that the ORR intermediates bind strongly on the bare metal site for Cr, Mn, and Ru metal atoms, especially on the MN$_4$C$_8$, MN$_3$C$_Z$, and MN$_3$C$_A$ structures. Thus, the ORR activity of the bare metal site locates on the left leg of the volcano plot, and the desorption of the *OH step restricts the reaction (ΔG$_4$). The *OH and *O ligand are found to decrease the ORR adsorption strength on the metal site, as previously found in the FeN$_y$C system. We find that the formation of OH ligand at the metal site enhance the ORR activity for the MN$_4$C$_{10}$, MN$_4$C$_Z$, MN$_4$C$_A$, and MN$_3$C$_{10}$ structure with the Mn and Cr metal atom while the *O ligand positively affects the ORR activity on the MN$_4$C$_8$, MN$_3$C$_Z$, and the MN$_3$C$_A$ structure with the Mn and Cr metal atom.

For the RuN$_y$C structures, we find that the formation of one *OH and *O ligand, which is expected under the working condition, is also beneficial for the ORR activity, especially *O. It turns out that the *O-Ru site has higher ORR activity than the bare metal site or the *OH-Ru site for the RuN$_4$C$_{10}$, RuN$_4$C$_8$, RuN$_4$C$_Z$, RuN$_4$C$_A$, RuN$_3$C$_Z$, and RuN$_3$C$_A$ structure.

The ORR intermediate adsorption on the bare Co metal site is weaker than the previous metal atoms. Still, the ORR intermediate strongly binds on the bare metal site in the MN$_4$C$_8$, MN$_3$C$_Z$, and MN$_3$C$_A$ structures. For the Co bare metal site, the ORR activity is still on the left leg of the volcano plot but locates near the peak of the volcano plot. The strong bonding of the *OH has restricted the reaction, except for the CoN$_4$C$_{12}$ structure where ΔG$_1$ limits the reaction. The *OH and *O ligands are found to decrease the ORR adsorption strength on the Co metal site. Unlike previously considered metal atoms, the effect of *OH and *O ligands on the Co metal site negatively affects the ORR activity on the CoN$_4$C$_{12}$, CoN$_4$C$_Z$, and CoN$_4$C$_A$ structure because the activity of the Co bare metal site is already near the top of the activity volcano. With *OH and *O ligands on these structures, the *OH adsorption strength is deceased, moving the active sites to the right leg of the volcano plot. However, under working conditions, the *OH ligand is expected to spontaneously evolve only on the Co metal site in the CoN$_3$C$_{10}$, CoN$_3$C$_Z$, and CoN$_3$C$_A$ structure which can substantially enhance the ORR activity.

In the NiN$_y$C structures, the ORR intermediate bond is too weak with the bare Ni metal site in most considered host carbon structures, and no *O and *OH ligands are expected on most NiN$_y$C sites. Thus, the first reaction step restricts the reaction (O$_2$ → *OOH; ΔG$_1$), and most NiN$_y$C structures are less active toward the ORR than other metal atoms, except for the NiN$_4$C$_8$ structure. The NiN$_4$C$_8$ structure turns out to have high ORR activity with the overpotential of 0.45 V$_{SHE}$. This is due to the stronger bonding between the Ni metal and the ORR intermediate on the NiN$_4$C$_8$ compared to other host structures.
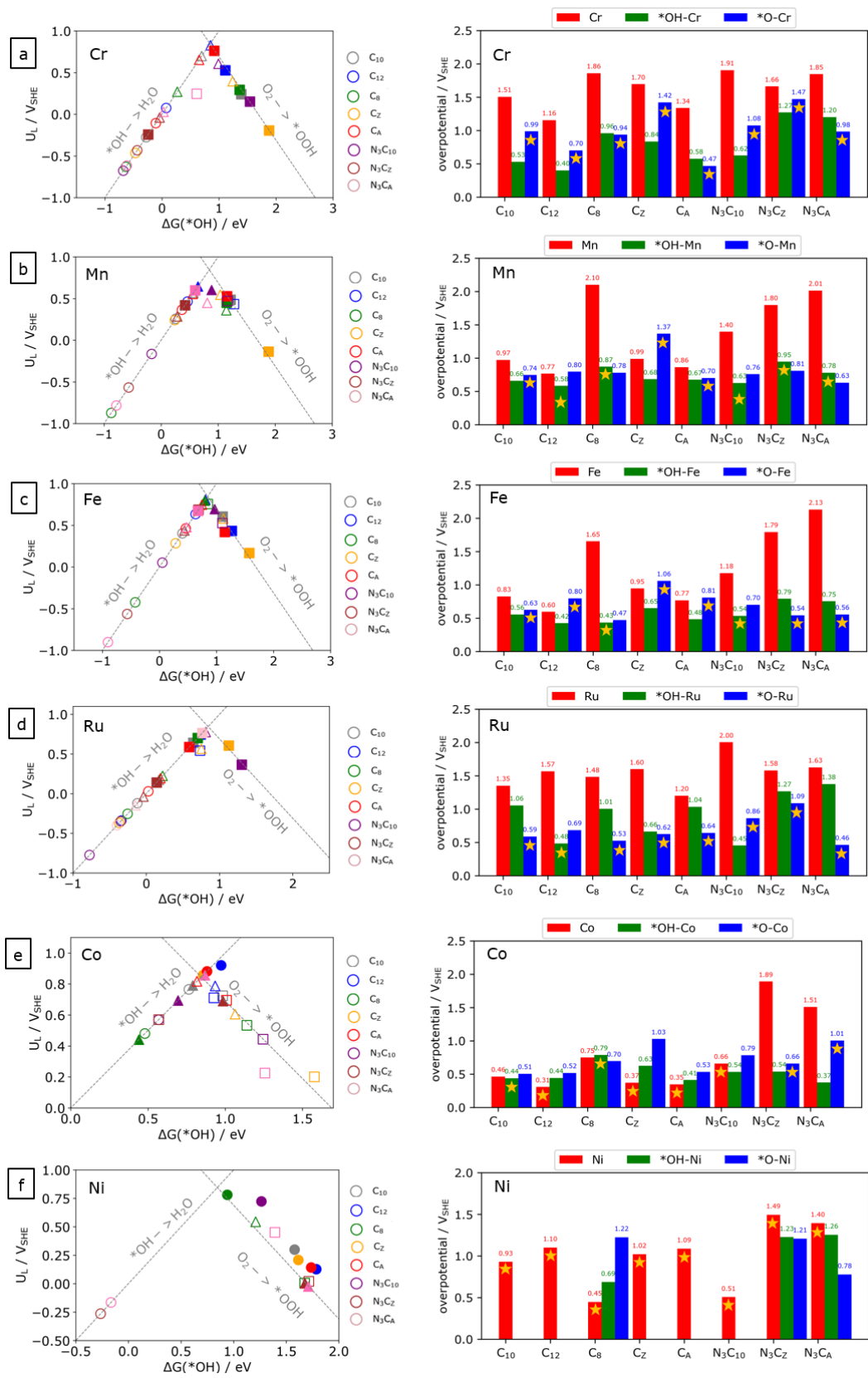
Figure 4: Limiting potential as a function of ΔG(*OH) (left) and ORR overpotential of the corresponding M-N-C systems (right): (a) Cr, (b) Co, (c) Mn, (d) Ni (e) Fe, and (f) Ru. The most stable phase at pH = 0 and U = 0.8 V_{SHE} are filled color and symbol for the surface: *M=circle,

*O-M=square, *OH-M=triangle in the volcano plot. The most stable phases are marks with a yellow star in the overpotential plot.

For the bare metal site, the binding energy of the ORR intermediate in the same carbon host structure is likely to follow the ordering (from strong to weak): Cr > Mn > Ru > Fe > Co > Ni. Among the different carbon host structures, the bare metal atom on the MN_4C_8, MN_3C_Z, MN_3C_A structure is likely to bond with the adsorbate too strongly. We find that in the optimized structure of the MN_4C_8 with an adsorbate, the metal atom is likely to lay above the basal plane, forming a distorted square-pyramidal geometry instead of a square-pyramidal geometry. Also, we find that the metal atom (with adsorbate) in this distorted square-pyramidal geometry prefers a higher spin state than in other structures with a square-pyramidal geometry.

Consider the FeN_4C_{12}, FeN_4C_{10}, and FeN_4C_8 structures as an example in Figure S24. The optimized structures of the FeN_4C_{12}, FeN_4C_{10}, and FeN_4C_8 are in a square planar geometry. The Fe^{+2} have a spin configuration with two (or almost two) unpaired d electrons in these structures. Due to the *OH adsorption, the d electron in the highest level is transferred to the *OH adsorbate. The *OH-FeN_4C_{12} and *OH-FeN_4C_{10} structures are in the square pyramidal geometry where the Fe^{+3} has only one unpaired electron in their orbital configuration. For the *OH-FeN_4C_8 structure, the *OH adsorption causes the elevation of the Fe metal about 0.80 Angstrom above the N_4 plane. The distortion could lead to a different orbital configuration, as suggested by Jurca et al. [73]. The possible d electron configuration in an orbital configuration associated with the distortion has three unpaired d electrons, resulting in a higher spin state configuration. The electron configuration in the *OH-FeN_4C_8 structure has lower energy than those in the *OH-FeN_4C_{12} and *OH-FeN_4C_{10} structure. Therefore, the *OH adsorption on the FeN_4C_8 is more energetically favorable than the FeN_4C_{12} and FeN_4C_{10} structure. The degree of distortion depends on the choice of the metal center. The distorted square-pyramidal geometry upon the intermediate adsorption also causes the high spin configuration on the Mn^{+3} and Co^{+3}, which also has strong binding energy with the adsorbate (Figure S25). There is no significant difference in the spin state of Cr^{+3} in the *OH-CrN_4C_8, *OH-CrN_4C_{12}, and *OH-CrN_4C_{10} structure since both geometries have the same three unpaired d-electrons; however, the elevation of the Cr metal atom in the *OH-CrN_4C_8 is relatively higher and the *OH adsorption is stronger compared to that of the CrN_4C_{10} and CrN_4C_{12} structure (Figure S26). The distorted square-pyramidal geometry may be the energetically favored structure. Like the Cr-N-C system, the Ni^{+3} has the same d electron configuration for both distorted and undistorted square-pyramidal geometry; thus, there is no different spin state among considered structures as observed in the previous Fe-N-C system, but the Ni site in the NiN_4C_8 structure still bonds with the adsorbate stronger than other structures. However, the Ni metal atom is unlikely to react with the ORR intermediate, so the evaluation of the Ni atom out of the N_4 plane upon the intermediate adsorption is relatively small compared to other MN_4C_8 structures. For the *OH-RuN_4C_8, the Ru metal atom with *OH adsorbate is about

0.97 Angstrom above the N_4 plane (Figure S27). The Ru^{+3} in the RuN_4C_8 structure also has a higher spin state and stronger *OH bonding than in the *OH-RuN_4C_{12} and *OH-RuN_4C_{10} structure.

Note that the pristine structure of the bulk-host (MN_4C_{10}) and edge-hosted MN_4 site (MN_4C_Z and MN_4C_A) is a square planar geometry. The metal center in these pristine structures has a similar converged magnetic moment on the metal atom (Table S10), implying a similar spin state. For the Fe-N-C system, the magnetic moment is 1.83, 1.92, and 1.91 for the pristine FeN_4C_{10}, FeN_4C_Z, and FeN_4C_A structures, respectively. The change in the d band center due the change in structure from the bulk-hosted MN_4 site to the edge-hosted MN_4 sites varies with the metal center element (Table S10). In the Fe-N-C system, the d-band center shifts up from -1.13 eV to -0.91 and -0.94 eV when the structure changes from the FeN_4C_{10} to the FeN_4C_Z and FeN_4C_A structure, respectively. While the *OH adsorption free energy is 0.40, 0.28 and 0.46 eV for the FeN_4C_{10}, FeN_4C_Z and FeN_4C_A structure respectively. In these cases, the adsorption of *OH is more energetically favorable on the zigzag edge host (FeN_4C_Z) structure than the others (FeN_4C_{10}, FeN_4C_A). After one *OH adsorption, the bulk-hosted MN_x site and edge-hosted MN_x sites adopt a square-pyramidal geometry. In the case of the Fe-N-C system, the elevation of the metal center upon the *OH adsorption is 0.28, 0.45, and 0.26 Å for the *OH-FeN_4C_{10}, *OH-FeN_4C_Z and *OH-FeN_4C_A structures, respectively (Figure S28) This elevation is significantly smaller than the elevation in the *OH-FeN_4C_8 structure, which is 0.80 Å. The magnetic moment on the metal atom is 1.17, 1.70, and 1.00 for the *OH-FeN_4C_{10}, *OH-FeN_4C_Z, and *OH-FeN_4C_A structures, respectively, resulting in a low spin configuration. The ORR activity can be found in Table S14 for the Fe-N-C system. The pristine FeN_4C_A structure, which the FeN_4 site located at the armchair edge, is slightly more active toward the ORR than the bulk-host FeN_4 site (overpotential is 0.08 V lower than the FeN_4C_{10} site). However, the ORR activity also depends on the *OH and *O ligands which can form in closed potential. With the *OH, the FeN_4 site at the armchair edge still has better ORR activity than the bulk-hosted one (overpotential is 0.08 V lower than the *OH-FeN_4C_{10} site)—however, the ORR activity order change with the *O ligand. The formation energies of the bulk-hosted and edged-host MN_4 sites are calculated and presented in Table S10. Our results suggest that forming the MN_4 site at the edge, either on a zigzag or armchair edge, is energetically favorable compared to forming it on the graphene bulk structure for all considered metal elements.

The MN_3C_Z and MN_3C_A structures are also likely to bond with the adsorbate strongly, regardless of the metal atom. This is possible because the metal atom has a possible oxidation state of +1 in these two structures. Thus, the metal atom prefers to form at least one more bond with the adsorbate, changing the oxidation from +1 to +2 or +3, which is generally favorable for transition metal atoms. To consider the NiN_3C_A and NiN_3C_Z structures as examples, see Table S11, we find that the pristine structures are converted into +1 spin states (one unpaired electron). The *O and *OH bond strongly with the bare Ni metal site in the NiN_4C_A and $NiN4C_Z$, and the spin states become +0, which is the same as other NiN_4C_y structures without adsorbates. The bonding with

another ORR intermediate as a second adsorbate on the NiN_3C_A and NiN_3C_Z structure becomes too weak, and it is comparable to that on the bare Ni atom on other NiN_4C_y structures. In other words, the metal atom in the MN_3C_A and MN_3C_Z structure is unsaturated and prefers to form a bond with the adsorbate. The preference of *O and *OH on these unsaturated structures is advantageous for Fe and Co catalysts. We find that *O strongly adsorbs on the FeN_3C_Z and FeN_3C_A structures and becomes a part of the active site where the theoretical overpotential can be as low as 0.54 and 0.56 $V_{SHE,}$ respectively. Similarly, the *OH-CoN_3C_Z and *OH-CoN_3C_A active sites can reach as low theoretical overpotential as 0.54 and 0.37 V_{SHE}.

3.3   Stability vs. activity

Combining the acid stability and activity descriptors, we plot the relative stability of the most stable phase at U = 0.8 V_{SHE}, pH = 0 against the ORR activity in Figure 5. We consider the structure with the relative stability lower than 1 eV and the overpotential less than 1 V_{SHE}. The stable and active sites shown in Figure 5 are from the Fe, Co, Ni, and Ru metal atom mainly on the graphene plane (both MN_4C_{10} and MN_3C_{10} structure) and at the edge of the graphene (Table 1). The MN_yC structure with Cr ad Mn metal atoms is predicted to be unstable under the considered condition as the thermodynamic driving force toward the dissolution is greater than 1 eV. Also, most MN_yC structures hosted by the micropore and the unsaturated MN_y structures that exhibit higher catalytic activity than the active site on the graphene plane for some metal atoms are not in Figure 5 due to the same reason.

Besides the well-known Fe-N-C catalyst, the Ru-N-C[74,75], Co-N-C[22,23,76,77], and Mn-N-C[78,79] catalysts have already been synthesized and tested as an ORR catalyst in acid conditions. However, when we compare theoretical and experimental results, we need to keep in mind that the variation in catalyst preparation and different metal precursor[80] can possibly lead to a different configuration of MN_y site for different metal atoms.

Xiao et al. has reported that the RuN_4 single-atom catalyst exhibits oxygen reduction reaction turnover frequency in 0.1 M $HClO_4$ exceeding the FeN_4 single atom in the same solution while the activity loss is less than that of the FeN_4 single atom[74]. Furthermore, the *OH-RuN_4 site has be suggested as an active site for the ORR activity in acid conditions[74]. The experimental study by Cao et al.[24] and Zhang et al.[75]. suggests that under working potential in acid solution, the active and stable site for the RuN_4 single-atom catalyst is the Ru metal site bond with an oxygen atom, in agreement with our finding. Furthermore, Zitolo et al.[23] has suggested that the Fe-based moieties experience structural change and electronic-state change, implying that the *O and *OH ligand originating from H_2O can exist under operating while it does not occur for the Co-based moieties. This partially agrees with this study. Most of the Fe-N-C sites have either one *O or *OH on one side of the Fe metal, while only some of the Co-N-C sites have the *O or *OH ligand at the ORR relevant condition.

We find that the stable CoN_yC structures in Table 1 and Figure 5 are more active than the stable FeN_yC structures. Previous experimental studies have reported that the Co-N-C catalyst exhibits high stability in acid condition[22,77]. However, Martinez et al. have found the ORR activity order in 0.5 H_2SO_4 to be Fe > Co > Mn[78]. To match the experimental results and DFT calculation, Martinez et al. have also suggested that the *OH ligand must be adsorbed on one side of the metal atom in the MN_4C_A. While not included in this study, it is well known that impurities or anions from the electrolyte can be adsorbed on an MN_4 motif site and can either enhance or deteriorate the catalytic activity[67,81]. The computational study by Svane et al. has found that the ligand under H_2SO_4 solution for the FeN_4C_{12} and MnN_4C_{12} structure is HSO_4 and H_2O for CoN_4C_{12} structure, giving good ORR catalytic activity (Fe > Co > Mn)[25] in agreement with the experimental trend in the same solution reported by Martinez et al. [78]. The interaction of the single metal site on different local carbon structures with the relevant species in the electrolyte should be further considered to create a model that can accurately describe both the catalytic activity and stability under experimental conditions[25,67]. Another possible explanation for this could be that the Co-N-C catalyst is highly selective for the two-electron pathway, potentially lowering catalytic activity for the four-electron pathway. Martinez et al. has reported that the Fe-N-C catalyst has a half-wave potential of 0.80 V_{RHE} and a selectively for four-electron pathway more than 95% while the Co-N-C catalyst has a lower half-wave potential of 0.77 V_{RHE} and lower selectively for four-electron path (90%)[78]. Similarly, Gao et al. has reported that the Co-N-C and Fe-N-C catalyst both show high onset potential at around 0.7 V_{RHE}, but the Co-N-C catalyst is more selective for the two-electron pathway than the Fe-N-C catalyst[82], also agreeing with Zitolo et al.[23].

Some of the promising stable and active structures in acid condition are the FeN_3C_{10}, CoN_3C_{10}, and NiN_3C_{10} structure, suggesting that the catalytic activity of the MN_x on the graphene plane can be tuned by the nearest neighbor interaction so careful manipulation of the heteroatoms around the active site can possibly further improve the catalytic activity of the MN_yC_{10} structure while maintaining acid stability. Additionally, for the design strategies to achieve both active site and stable M-N-C catalyst, the synthesized aim should be increasing the site density of MN_x bulk-hosted structures (MN_4C_{10} or MN_3C_{10}) or the MN_4 on the edge-hosted graphene structure. Also, avoiding the formation of unsaturated MN_3C_Z or MN_3C_A structure as well as the MN_4C_8 site, which bridged between two armchair edges will increase the stability of the M-N-C catalyst under acid conditions. Further stability improvement for the active M-N-C structures hosted by the micropores (MN_4C_{12}, MN_4C_8) or the unsaturated structure (MN_3C_Z, MN_3C_A) might be achieved by forming these active structures over another graphitic layer. The metal choice also significantly affects both stability and activity and should be considered when designing the catalyst. Integrating Fe, Co, and Ru metal elements into graphitic carbon supports like the MN_xC_{10} structure would be a promising catalyst for the ORR in acid conditions.
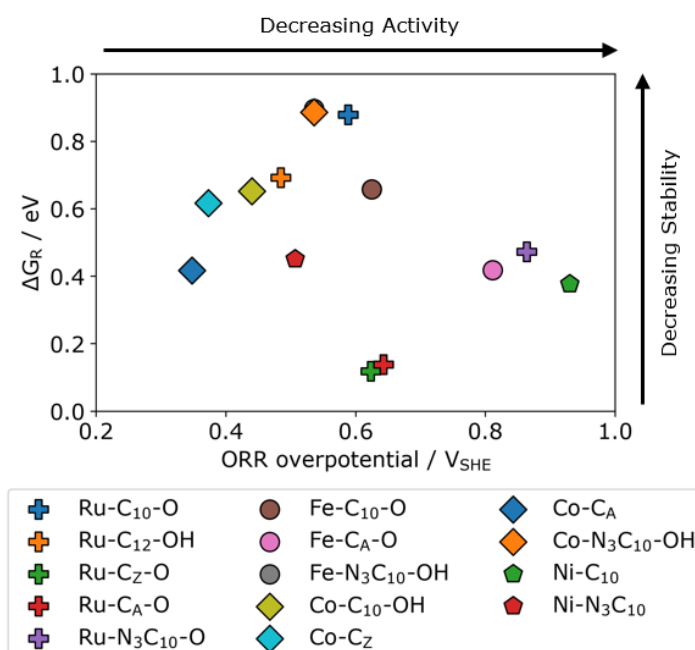
Figure 5: Relative stability of the most stable phase at $U = 0.8$ V_{SHE} and pH = 0 vs. theoretical ORR overpotential with nonadsorbing electrolyte ions. The catalysts close to the bottom left corner are expected to be active toward ORR and stable in acid conditions.

Table 1: Promising structures with the ORR overpotential less than 1 V_{SHE} and relative stability at $U = 0.8$ V_{SHE} and pH = 0 less than 1.0 eV.

System	Active site	ΔG_R / eV	overpotential / V_{SHE}
RuN_4C_{10}	*O-Ru	0.88	0.59
RuN_4C_{12}	*OH-Ru	0.69	0.49
RuN_4C_Z	*O-Ru	0.12	0.62
RuN_4C_A	*O-Ru	0.14	0.64
RuN_3C_{10}	*O-Ru	0.47	0.86
FeN_4C_{10}	*O-Fe	0.66	0.63
FeN_4C_A	*O-Fe	0.42	0.81
FeN_3C_{10}	*OH-Fe	0.90	0.54
CoN_4C_{10}	*OH-Co	0.65	0.44
CoN_4C_Z	*Co	0.62	0.37
CoN_4C_A	*Co	0.42	0.35
CoN_3C_{10}	*OH-Co	0.89	0.54
NiN_4C_{10}	*Ni	0.38	0.93
NiN_3C_{10}	*Ni	0.45	0.51

3. Conclusion

To summarize, we have systematically investigated stabilities and ORR catalytic activity of the MN_x site on different local atomic structures in acid conditions using DFT calculations, which reveal that the local atomic structure plays a crucial role in both stability and ORR catalytic activity. The stability is here considered from the tendency of a single metal atom to dissolve into the electrolyte. The calculation reveals that all considered MN_x structures are thermodynamically unstable in acid ORR conditions. The thermodynamic driving forces toward the dissolution suggest that the single metal site on the graphene plane and at the edge of the graphene (MN_yC_{10}, MN_yC_A, and MN_yC_Z) are more stable against the dissolution than the single metal sites host by the microporous (i.e., MN_4C_{12}, MN_4C_8) or in the unsaturated single metal site at the edge (MN_3C_Z and MN_3C_A). The stability also depends on the choice of metal site. The MN_x sites with Fe, Co, Ni, and Ru metal atoms are more stable under the acid conditions than those with Mn and Cr metal atoms. Under reaction conditions, we predict the most stable phase of the active site in which *O or *OH ligands occur and become a part of the active site. The ORR activity also depends on the choice of metal and the local atomic structure around the metal site. The MN_4C_8, MN_3C_Z, and MN_3C_A structures are likely to bond with the intermediate too strongly, generally having one *O or *OH ligand on the metal site. For different metal atoms, the Cr, Mn, Ru, and Fe metal bond with the ORR intermediate quite strongly, and the ORR occurs with *O or *OH ligands. The bonding strength becomes weak for the Ni metal atom compared to other considered metal atoms, and most considered structures with Ni are not active toward ORR. Combining both stability and activity descriptors, we identify that single Fe, Co, and Ru metal atoms mostly on the MN_4C_{10}, MN_4C_Z, MN_4C_A, and MN_3C_{10} structure are the promising acid-stable active ORR catalyst. Therefore, rational modification of carbon matrix hosting MN_y moieties and appropriate selection of a metal atom could be carefully used to optimize the activity and stability toward the reaction. This computational study provides useful guidance to rational design and controlled synthesis of M-N-C electrocatalyst to achieve both active and stable catalyst under working conditions not only for the ORR but also the OER due to their similar operating conditions and reaction intermediates. Our study highlights the improved stability of MN_4C_{10}, MN_4C_Z, and MN_4C_A sites against the demetallation and metal clustering compared to, e.g., MN_4C_8 and MN_4C_{12} sites. The approach can be further applied to the N_2[83] and CO_2 reduction reactions[84,85], and refined by including relevant reaction intermediates such as *H, *CO, and *NH_3 at the more reducing reaction conditions. Figure S30 is an example of extending stability diagrams and relative stability plots at different pH, showing that the approach is flexible and can be applied for varied electrochemical environments. Furthermore, these computational approaches are of interest to the further understanding of acid stability of other geometries of M−N−C materials, such as the dual metal site embedded on the graphene[61,63,86] or a diporphyrin complex[84,87].

Supporting Information

Images of optimized structures; Free energy of dissolved metal ions; stability diagrams of the Fe-N-C system; protonation free reaction energy at the metal dissolved carbon cavity; dissolution potential to Fe^{+2}; free adsorption energy of ORR intermediates, the relative stability of Fe, *OH-Fe, *O-Fe with different unit cells and solvation models; stability diagrams for Fe-N-C, Cr-N-C, Mn-N-C, Co-N-C, Ni-N-C, Ru-N-C, Pt-N-C systems; the energy of the MN_x site against metal clustering and energy for oxidizing metal atom; stability diagrams and relative stability for Fe-N-C system with nearby *O, *OH and graphitic N atoms; orbital splitting of d-state and occupancy; possible oxidation and spin state of Ni-N-C system; d-band center and formation energy for the bulk-hosted and edged hosted MN_x site; adsorption free energy of ORR intermediates, ORR overpotentials and relative stability for Fe-N-C, Cr-N-C, Mn-N-C, Co-N-C, Ni-N-C, Ru-N-C, and Pt-N-C system.

References

(1)   Nørskov, J. K.; Rossmeisl, J.; Logadottir, A.; Lindqvist, L.; Kitchin, J. R.; Bligaard, T.; Jónsson, H. Origin of the Overpotential for Oxygen Reduction at a Fuel-Cell Cathode. *J. Phys. Chem. B* **2004**, *108* (46), 17886–17892. https://doi.org/10.1021/jp047349j.

(2)   Peng, B.; Liu, H.; Liu, Z.; Duan, X.; Huang, Y. Toward Rational Design of Single-Atom Catalysts. *J. Phys. Chem. Lett.* **2021**, *12* (11), 2837–2847. https://doi.org/10.1021/acs.jpclett.1c00049.

(3)   He, Y.; Liu, S.; Priest, C.; Shi, Q.; Wu, G. Atomically Dispersed Metal-Nitrogen-Carbon Catalysts for Fuel Cells: Advances in Catalyst Design, Electrode Performance, and Durability Improvement. *Chem. Soc. Rev.* **2020**, *49* (11), 3484–3524. https://doi.org/10.1039/c9cs00903e.

(4)   Kaiser, S. K.; Chen, Z.; Faust Akl, D.; Mitchell, S.; Pérez-Ramírez, J. Single-Atom Catalysts across the Periodic Table. *Chem. Rev.* **2020**, *120* (21), 11703–11809. https://doi.org/10.1021/acs.chemrev.0c00576.

(5)   Osmieri, L.; Cullen, D. A.; Chung, H. T.; Ahluwalia, R. K.; Neyerlin, K. C. Durability Evaluation of a Fe–N–C Catalyst in Polymer Electrolyte Fuel Cell Environment via Accelerated Stress Tests. *Nano Energy* **2020**, *78* (August), 105209. https://doi.org/10.1016/j.nanoen.2020.105209.

(6)   Ramaswamy, N.; Hakim, N.; Mukerjee, S. Degradation Mechanism Study of Perfluorinated Proton Exchange Membrane under Fuel Cell Operating Conditions.

Electrochim. Acta **2008**, *53* (8), 3279–3295.
https://doi.org/10.1016/j.electacta.2007.11.010.

(7)   Choi, C. H.; Lim, H. K.; Chung, M. W.; Chon, G.; Ranjbar Sahraie, N.; Altin, A.; Sougrati,
      M. T.; Stievano, L.; Oh, H. S.; Park, E. S.; Luo, F.; Strasser, P.; Dražić, G.; Mayrhofer, K.
      J. J.; Kim, H.; Jaouen, F. The Achilles' Heel of Iron-Based Catalysts during Oxygen
      Reduction in an Acidic Medium. *Energy Environ. Sci.* **2018**, *11* (11), 3176–3182.
      https://doi.org/10.1039/c8ee01855c.

(8)   Nabae, Y.; Yuan, Q.; Nagata, S.; Kusaba, K.; Aoki, T.; Takao, N.; Itoh, T.; Arao, M.;
      Imai, H.; Higashi, K.; Sakata, T.; Uruga, T.; Iwasawa, Y. In Situ X-Ray Absorption
      Spectroscopy to Monitor the Degradation of Fe/N/C Cathode Catalyst in Proton Exchange
      Membrane Fuel Cells. *J. Electrochem. Soc.* **2021**, *168* (1), 014513.
      https://doi.org/10.1149/1945-7111/abdc64.

(9)   Chen, Z.; Jiang, S.; Kang, G.; Nguyen, D.; Schatz, G. C.; Van Duyne, R. P. Operando
      Characterization of Iron Phthalocyanine Deactivation during Oxygen Reduction Reaction
      Using Electrochemical Tip-Enhanced Raman Spectroscopy. *J. Am. Chem. Soc.* **2019**, *141*
      (39), 15684–15692. https://doi.org/10.1021/jacs.9b07979.

(10) Goellner, V.; Baldizzone, C.; Schuppert, A.; Sougrati, M. T.; Mayrhofer, K.; Jaouen, F.
      Degradation of Fe/N/C Catalysts upon High Polarization in Acid Medium. *Phys. Chem.*
      Chem. Phys. **2014**, *16* (34), 18454–18462. https://doi.org/10.1039/c4cp02882a.

(11) Kumar, K.; Asset, T.; Li, X.; Liu, Y.; Yan, X.; Chen, Y.; Mermoux, M.; Pan, X.; Atanassov,
      P.; Maillard, F.; Dubau, L. Fe-N-C Electrocatalysts' Durability: Effects of Single Atoms'
      Mobility and Clustering. *ACS Catal.* **2021**, *11* (2), 484–494.
      https://doi.org/10.1021/acscatal.0c04625.

(12) Santori, P. G.; Speck, F. D.; Li, J.; Zitolo, A.; Jia, Q.; Mukerjee, S.; Cherevko, S.; Jaouen,
      F. Effect of Pyrolysis Atmosphere and Electrolyte PH on the Oxygen Reduction Activity,
      Stability and Spectroscopic Signature of FeN x Moieties in Fe-N-C Catalysts . *J.*
      Electrochem. Soc. **2019**, *166* (7), F3311–F3320. https://doi.org/10.1149/2.0371907jes.

(13) Zitolo, A.; Goellner, V.; Armel, V.; Sougrati, M. T.; Mineva, T.; Stievano, L.; Fonda, E.;
      Jaouen, F. Identification of Catalytic Sites for Oxygen Reduction in Iron- and Nitrogen-
      Doped Graphene Materials. *Nat. Mater.* **2015**, *14* (9), 937–942.
      https://doi.org/10.1038/nmat4367.

(14) Lefèvre, M.; Proietti, E.; Jaouen, F.; Dodelet, J. P. Iron-Based Catalysts with Improved
      Oxygen Reduction Activity in Polymer Electrolyte Fuel Cells. *Science (80-.).* **2009**, *324*
      (5923), 71–74. https://doi.org/10.1126/science.1170051.

(15) Kramm, U. I.; Herranz, J.; Larouche, N.; Arruda, T. M.; Lefèvre, M.; Jaouen, F.;
      Bogdanoff, P.; Fiechter, S.; Abs-Wurmbach, I.; Mukerjee, S.; Dodelet, J. P. Structure of
      the Catalytic Sites in Fe/N/C-Catalysts for O 2-Reduction in PEM Fuel Cells. *Phys. Chem.*
      Chem. Phys. **2012**, *14* (33), 11673–11688. https://doi.org/10.1039/c2cp41957b.

(16) Chenitz, R.; Kramm, U. I.; Lefèvre, M.; Glibin, V.; Zhang, G.; Sun, S.; Dodelet, J. P. A Specific Demetalation of Fe-N4 Catalytic Sites in the Micropores of NC-Ar + NH3 Is at the Origin of the Initial Activity Loss of the Highly Active Fe/N/C Catalyst Used for the Reduction of Oxygen in PEM Fuel Cells. *Energy Environ. Sci.* **2018**, *11* (2), 365–382. https://doi.org/10.1039/c7ee02302b.

(17) Liu, K.; Wu, G.; Wang, G. Role of Local Carbon Structure Surrounding FeN4 Sites in Boosting the Catalytic Activity for Oxygen Reduction. *J. Phys. Chem. C* **2017**, *121* (21), 11319–11324. https://doi.org/10.1021/acs.jpcc.7b00913.

(18) Zhang, H.; Chung, H. T.; Cullen, D. A.; Wagner, S.; Kramm, U. I.; More, K. L.; Zelenay, P.; Wu, G. High-Performance Fuel Cell Cathodes Exclusively Containing Atomically Dispersed Iron Active Sites. *Energy Environ. Sci.* **2019**, *12* (8), 2548–2558. https://doi.org/10.1039/c9ee00877b.

(19) Li, J.; Sougrati, M. T.; Zitolo, A.; Ablett, J. M.; Oğuz, I. C.; Mineva, T.; Matanovic, I.; Atanassov, P.; Huang, Y.; Zenyuk, I.; Di Cicco, A.; Kumar, K.; Dubau, L.; Maillard, F.; Dražić, G.; Jaouen, F. Identification of Durable and Non-Durable FeNx Sites in Fe−N−C Materials for Proton Exchange Membrane Fuel Cells. *Nat. Catal.* **2021**, *4* (1), 10–19. https://doi.org/10.1038/s41929-020-00545-2.

(20) Speck, F. D.; Paul, M. T. Y.; Ruiz-Zepeda, F.; Gatalo, M.; Kim, H.; Kwon, H. C.; Mayrhofer, K. J. J.; Choi, M.; Choi, C. H.; Hodnik, N.; Cherevko, S. Atomistic Insights into the Stability of Pt Single-Atom Electrocatalysts. *J. Am. Chem. Soc.* **2020**, *142* (36), 15496–15504. https://doi.org/10.1021/jacs.0c07138.

(21) Gubler, L.; Dockheer, S. M.; Koppenol, W. H. Radical (HO•, H• and HOO•) Formation and Ionomer Degradation in Polymer Electrolyte Fuel Cells. *J. Electrochem. Soc.* **2011**, *158* (7), B755. https://doi.org/10.1149/1.3581040.

(22) Xie, X.; He, C.; Li, B.; He, Y.; Cullen, D. A.; Wegener, E. C.; Kropf, A. J.; Martinez, U.; Cheng, Y.; Engelhard, M. H.; Bowden, M. E.; Song, M.; Lemmon, T.; Li, X. S.; Nie, Z.; Liu, J.; Myers, D. J.; Zelenay, P.; Wang, G.; Wu, G.; Ramani, V.; Shao, Y. Performance Enhancement and Degradation Mechanism Identification of a Single-Atom Co−N−C Catalyst for Proton Exchange Membrane Fuel Cells. *Nat. Catal.* **2020**, *3* (12), 1044–1054. https://doi.org/10.1038/s41929-020-00546-1.

(23) Zitolo, A.; Ranjbar-Sahraie, N.; Mineva, T.; Li, J.; Jia, Q.; Stamatin, S.; Harrington, G. F.; Lyth, S. M.; Krtil, P.; Mukerjee, S.; Fonda, E.; Jaouen, F. Identification of Catalytic Sites in Cobalt-Nitrogen-Carbon Materials for the Oxygen Reduction Reaction. *Nat. Commun.* **2017**, *8* (1), 957. https://doi.org/10.1038/s41467-017-01100-7.

(24) Cao, L.; Luo, Q.; Chen, J.; Wang, L.; Lin, Y.; Wang, H.; Liu, X.; Shen, X.; Zhang, W.; Liu, W.; Qi, Z.; Jiang, Z.; Yang, J.; Yao, T. Dynamic Oxygen Adsorption on Single-Atomic Ruthenium Catalyst with High Performance for Acidic Oxygen Evolution Reaction. *Nat. Commun.* **2019**, *10* (1), 4849. https://doi.org/10.1038/s41467-019-12886-z.

(25) Svane, K. L.; Reda, M.; Vegge, T.; Hansen, H. A. Improving the Activity of M−N4 Catalysts for the Oxygen Reduction Reaction by Electrolyte Adsorption. *ChemSusChem* **2019**, *12* (23), 5133–5141. https://doi.org/10.1002/cssc.201902443.

(26) Zhao, C.; Gao, W.; Jiang, Q. Scheme for Screening O2 Reduction Electrocatalysts: From Pure Metals and Alloys to Single-Atom Catalysts. *J. Phys. Chem. C* **2020**, *124* (46), 25412–25420. https://doi.org/10.1021/acs.jpcc.0c08344.

(27) Deng, Q.; Zhao, J.; Wu, T.; Chen, G.; Hansen, H. A.; Vegge, T. 2D Transition Metal–TCNQ Sheets as Bifunctional Single-Atom Catalysts for Oxygen Reduction and Evolution Reaction (ORR/OER). *J. Catal.* **2019**, *370*, 378–384. https://doi.org/10.1016/j.jcat.2018.12.012.

(28) Hansen, H. A.; Shi, C.; Lausche, A. C.; Peterson, A. A.; Nørskov, J. K. Bifunctional Alloys for the Electroreduction of CO2 and CO. *Phys. Chem. Chem. Phys.* **2016**, *18* (13), 9194–9201. https://doi.org/10.1039/c5cp07717f.

(29) Hansen, H. A.; Rossmeisl, J.; Nørskov, J. K. Surface Pourbaix Diagrams and Oxygen Reduction Activity of Pt(111), Ag(111) and Ni(111) Surfaces Studied by DFT. *Phys. Chem. Chem. Phys.* **2008**, *10* (25), 3722–3730. https://doi.org/10.1039/B803956A.

(30) Hubert, M. A.; Patel, A. M.; Gallo, A.; Liu, Y.; Valle, E.; Ben-Naim, M.; Sanchez, J.; Sokaras, D.; Sinclair, R.; Nørskov, J. K.; King, L. A.; Bajdich, M.; Jaramillo, T. F. Acidic Oxygen Evolution Reaction Activity-Stability Relationships in Ru-Based Pyrochlores. *ACS Catal.* **2020**, *10* (20), 12182–12196. https://doi.org/10.1021/acscatal.0c02252.

(31) Gunasooriya, G. T. K. K.; Nørskov, J. K. Analysis of Acid-Stable and Active Oxides for the Oxygen Evolution Reaction. *ACS Energy Lett.* **2020**, *5* (12), 3778–3787. https://doi.org/10.1021/acsenergylett.0c02030.

(32) Calle-Vallejo, F.; Martínez, J. I.; García-Lastra, J. M.; Abad, E.; Koper, M. T. M. Oxygen Reduction and Evolution at Single-Metal Active Sites: Comparison between Functionalized Graphitic Materials and Protoporphyrins. *Surf. Sci.* **2013**, *607*, 47–53. https://doi.org/10.1016/j.susc.2012.08.005.

(33) Zhou, Y.; Gao, G.; Chu, W.; Wang, L. W. Computational Screening of Transition Metal-Doped Phthalocyanine Monolayers for Oxygen Evolution and Reduction. *Nanoscale Adv.* **2020**, *2* (2), 710–716. https://doi.org/10.1039/c9na00648f.

(34) Ha, M.; Kim, D. Y.; Umer, M.; Gladkikh, V.; Myung, C. W.; Kim, K. S. Tuning Metal Single Atoms Embedded in NxCy Moieties toward High-Performance Electrocatalysis. *Energy Environ. Sci.* **2021**, *14* (6), 3455–3468. https://doi.org/10.1039/d1ee00154j.

(35) Back, S.; Siahrostami, S. Noble Metal Supported Hexagonal Boron Nitride for the Oxygen Reduction Reaction: A DFT Study. *Nanoscale Adv.* **2019**, *1* (1), 132–139. https://doi.org/10.1039/c8na00059j.

(36) Glibin, V. P.; Dodelet, J.-P. Thermodynamic Stability in Acid Media of FeN 4 -Based Catalytic Sites Used for the Reaction of Oxygen Reduction in PEM Fuel Cells . *J.*

Electrochem. Soc. **2017**, *164* (9), F948–F957. https://doi.org/10.1149/2.1041709jes.

(37) Yin, X.; Holby, E. F.; Zelenay, P. Comment on 'Non-PGM Electrocatalysts for PEM Fuel Cells: Effect of Fluorination on the Activity and Stability of a Highly Active NC_Ar + NH3catalyst' by Gaixia Zhang, Xiaohua Yang, Marc Dubois, Michael Herraiz, Régis Chenitz, Michel Lefèvre, Mohamed Cheri. *Energy Environ. Sci.* **2021**, *14* (2), 1029–1033. https://doi.org/10.1039/d0ee02069a.

(38) Holby, E. F.; Wang, G.; Zelenay, P. Acid Stability and Demetalation of PGM-Free ORR Electrocatalyst Structures from Density Functional Theory: A Model for "Single-Atom Catalyst" Dissolution. *ACS Catal.* **2020**, *10* (24), 14527–14539. https://doi.org/10.1021/acscatal.0c02856.

(39) Tan, X.; Tahini, H. A.; Smith, S. C. Unveiling the Role of Carbon Oxidation in Irreversible Degradation of Atomically-Dispersed FeN4moieties for Proton Exchange Membrane Fuel Cells. *J. Mater. Chem. A* **2021**, *9* (13), 8721–8729. https://doi.org/10.1039/d0ta12105c.

(40) Singh, A. K.; Zhou, L.; Shinde, A.; Suram, S. K.; Montoya, J. H.; Winston, D.; Gregoire, J. M.; Persson, K. A. Electrochemical Stability of Metastable Materials. *Chem. Mater.* **2017**, *29* (23), 10159–10167. https://doi.org/10.1021/acs.chemmater.7b03980.

(41) Kresse, G.; Hafner, J. Ab Initio Molecular Dynamics for Liquid Metals. *Phys. Rev. B* **1993**, *47* (1), 558–561. https://doi.org/10.1103/PhysRevB.47.558.

(42) Blöchl, P. E. Projector Augmented-Wave Method. *Phys. Rev. B* **1994**, *50* (24), 17953–17979. https://doi.org/10.1103/PhysRevB.50.17953.

(43) Hjorth Larsen, A.; JØrgen Mortensen, J.; Blomqvist, J.; Castelli, I. E.; Christensen, R.; Dułak, M.; Friis, J.; Groves, M. N.; Hammer, B.; Hargus, C.; Hermes, E. D.; Jennings, P. C.; Bjerre Jensen, P.; Kermode, J.; Kitchin, J. R.; Leonhard Kolsbjerg, E.; Kubal, J.; Kaasbjerg, K.; Lysgaard, S.; Bergmann Maronsson, J.; Maxson, T.; Olsen, T.; Pastewka, L.; Peterson, A.; Rostgaard, C.; SchiØtz, J.; Schütt, O.; Strange, M.; Thygesen, K. S.; Vegge, T.; Vilhelmsen, L.; Walter, M.; Zeng, Z.; Jacobsen, K. W. The Atomic Simulation Environment - A Python Library for Working with Atoms. *J. Phys. Condens. Matter* **2017**, *29* (27), 273002. https://doi.org/10.1088/1361-648X/aa680e.

(44) Wellendorff, J.; Lundgaard, K. T.; M\ogelh\oj, A.; Petzold, V.; Landis, D. D.; N\orskov, J. K.; Bligaard, T.; Jacobsen, K. W. Density Functionals for Surface Science: Exchange-Correlation Model Development with Bayesian Error Estimation. *Phys. Rev. B* **2012**, *85* (23), 235149. https://doi.org/10.1103/PhysRevB.85.235149.

(45) Mortensen, J.; Gjerding, M.; Thygesen, K. MyQueue: Task and Workflow Scheduling System. *J. Open Source Softw.* **2020**, *5* (45), 1844. https://doi.org/10.21105/joss.01844.

(46) Charreteur, F.; Jaouen, F.; Ruggeri, S.; Dodelet, J. P. Fe/N/C Non-Precious Catalysts for PEM Fuel Cells: Influence of the Structural Parameters of Pristine Commercial Carbon Blacks on Their Activity for Oxygen Reduction. *Electrochim. Acta* **2008**, *53* (6), 2925–

2938. https://doi.org/10.1016/j.electacta.2007.11.002.

(47) Cheng, Y.; Zhao, S.; Li, H.; He, S.; Veder, J. P.; Johannessen, B.; Xiao, J.; Lu, S.; Pan, J.; Chisholm, M. F.; Yang, S. Z.; Liu, C.; Chen, J. G.; Jiang, S. P. Unsaturated Edge-Anchored Ni Single Atoms on Porous Microwave Exfoliated Graphene Oxide for Electrochemical CO2. *Appl. Catal. B Environ.* **2019**, *243* (June 2018), 294–303. https://doi.org/10.1016/j.apcatb.2018.10.046.

(48) Monkhorst, H. J.; Pack, J. D. Special Points for Brillouin-Zone Integrations. *Phys. Rev. B* **1976**, *13* (12), 5188–5192. https://doi.org/10.1103/PhysRevB.13.5188.

(49) Mathew, K.; Sundararaman, R.; Letchworth-Weaver, K.; Arias, T. A.; Hennig, R. G. Implicit Solvation Model for Density-Functional Study of Nanocrystal Surfaces and Reaction Pathways. *J. Chem. Phys.* **2014**, *140* (8), 84106. https://doi.org/10.1063/1.4865107.

(50) Mathew, K.; Kolluru, V. S. C.; Mula, S.; Steinmann, S. N.; Hennig, R. G. Implicit Self-Consistent Electrolyte Model in Plane-Wave Density-Functional Theory. *J. Chem. Phys.* **2019**, *151* (23), 1–8. https://doi.org/10.1063/1.5132354.

(51) Goedecker, S. Minima Hopping: An Efficient Search Method for the Global Minimum of the Potential Energy Surface of Complex Molecular Systems. *J. Chem. Phys.* **2004**, *120* (21), 9911–9917. https://doi.org/10.1063/1.1724816.

(52) Goedecker, S.; Hellmann, W.; Lenosky, T. Global Minimum Determination of the Born-Oppenheimer Surface within Density Functional Theory. *Phys. Rev. Lett.* **2005**, *95* (5), 55501. https://doi.org/10.1103/PhysRevLett.95.055501.

(53) Peterson, A. A. Global Optimization of Adsorbate-Surface Structures While Preserving Molecular Identity. *Top. Catal.* **2014**, *57* (1–4), 40–53. https://doi.org/10.1007/s11244-013-0161-8.

(54) Kulkarni, A.; Siahrostami, S.; Patel, A.; Nørskov, J. K. Understanding Catalytic Activity Trends in the Oxygen Reduction Reaction. *Chem. Rev.* **2018**, *118* (5), 2302–2312. https://doi.org/10.1021/acs.chemrev.7b00488.

(55) Christensen, R.; Hansen, H. A.; Dickens, C. F.; Nørskov, J. K.; Vegge, T. Functional Independent Scaling Relation for ORR/OER Catalysts. *J. Phys. Chem. C* **2016**, *120* (43), 24910–24916. https://doi.org/10.1021/acs.jpcc.6b09141.

(56) Christensen, R.; Hansen, H. A.; Vegge, T. Identifying Systematic DFT Errors in Catalytic Reactions. *Catal. Sci. Technol.* **2015**, *5* (11), 4946–4949. https://doi.org/10.1039/c5cy01332a.

(57) Haynes, W. M. *CRC Handbook of Chemistry and Physics, 94th Edition*; Taylor & Francis, 2013; p 2668 pages.

(58) Pourbaix, M. *Atlas of Electrochemical Equilibria in Aqueous Solutions*, 2nd ed.; National Association of Corrosion Engineers: Houston, 1974; p 644.

(59) Bratsch, S. G. Standard Electrode Potentials and Temperature Coefficients in Water at

298.15 K. *J. Phys. Chem. Ref. Data* **1989**, *18* (1), 1–21. https://doi.org/10.1063/1.555839.

(60)　Hansen, H. A.; Viswanathan, V.; NØrskov, J. K. Unifying Kinetic and Thermodynamic Analysis of 2 E- and 4 e - Reduction of Oxygen on Metal Surfaces. *J. Phys. Chem. C* **2014**, *118* (13), 6706–6718. https://doi.org/10.1021/jp4100608.

(61)　Sahraie, N. R.; Kramm, U. I.; Steinberg, J.; Zhang, Y.; Thomas, A.; Reier, T.; Paraknowitsch, J.-P.; Strasser, P. Quantifying the Density and Utilization of Active Sites in Non-Precious Metal Oxygen Electroreduction Catalysts. *Nat. Commun.* **2015**, *6*, 8618. https://doi.org/10.1038/ncomms9618.

(62)　Lefèvre, M.; Dodelet, J. P. Fe-Based Catalysts for the Reduction of Oxygen in Polymer Electrolyte Membrane Fuel Cell Conditions: Determination of the Amount of Peroxide Released during Electroreduction and Its Influence on the Stability of the Catalysts. *Electrochim. Acta* **2003**, *48* (19), 2749–2760. https://doi.org/10.1016/S0013-4686(03)00393-1.

(63)　Svane, K. L.; Hansen, H. A.; Vegge, T. A Comparison of Single and Double Co Sites Incorporated in N-Doped Graphene for the Oxygen Reduction Reaction. *J. Catal.* **2021**, *393*, 230–237. https://doi.org/https://doi.org/10.1016/j.jcat.2020.11.024.

(64)　Zhang, Q.; Tan, X.; Bedford, N. M.; Han, Z.; Thomsen, L.; Smith, S.; Amal, R.; Lu, X. Direct Insights into the Role of Epoxy Groups on Cobalt Sites for Acidic H2O2 Production. *Nat. Commun.* **2020**, *11* (1), 4181. https://doi.org/10.1038/s41467-020-17782-5.

(65)　Jung, E.; Shin, H.; Lee, B. H.; Efremov, V.; Lee, S.; Lee, H. S.; Kim, J.; Hooch Antink, W.; Park, S.; Lee, K. S.; Cho, S. P.; Yoo, J. S.; Sung, Y. E.; Hyeon, T. Atomic-Level Tuning of Co–N–C Catalyst for High-Performance Electrochemical H2O2 Production. *Nat. Mater.* **2020**, *19* (4), 436–442. https://doi.org/10.1038/s41563-019-0571-5.

(66)　Xia, D.; Yang, X.; Xie, L.; Wei, Y.; Jiang, W.; Dou, M.; Li, X.; Li, J.; Gan, L.; Kang, F. Direct Growth of Carbon Nanotubes Doped with Single Atomic Fe–N4 Active Sites and Neighboring Graphitic Nitrogen for Efficient and Stable Oxygen Reduction Electrocatalysis. *Adv. Funct. Mater.* **2019**, *29* (49), 1–10. https://doi.org/10.1002/adfm.201906174.

(67)　Holst-Olesen, K.; Reda, M.; Hansen, H. A.; Vegge, T.; Arenz, M. Enhanced Oxygen Reduction Activity by Selective Anion Adsorption on Non-Precious-Metal Catalysts. *ACS Catal.* **2018**, *8* (8), 7104–7112. https://doi.org/10.1021/acscatal.8b01584.

(68)　Viswanathan, V.; Hansen, H. A.; Rossmeisl, J.; Nørskov, J. K. Universality in Oxygen Reduction Electrocatalysis on Metal Surfaces. *ACS Catal.* **2012**, *2* (8), 1654–1660. https://doi.org/10.1021/cs300227s.

(69)　Yang, X.; Xia, D.; Kang, Y.; Du, H.; Kang, F.; Gan, L.; Li, J. Unveiling the Axial Hydroxyl Ligand on Fe-N4-C Electrocatalysts and Its Impact on the PH-Dependent Oxygen Reduction Activities and Poisoning Kinetics. *Adv. Sci.* **2020**, *7* (12), 1–6. https://doi.org/10.1002/advs.202000176.

(70) Wang, Y.; Tang, Y.-J.; Zhou, K. Self-Adjusting Activity Induced by Intrinsic Reaction Intermediate in Fe–N–C Single-Atom Catalysts. *J. Am. Chem. Soc.* **2019**, *141* (36), 14115–14119. https://doi.org/10.1021/jacs.9b07712.

(71) Chung, H. T.; Cullen, D. A.; Higgins, D.; Sneed, B. T.; Holby, E. F.; More, K. L.; Zelenay, P. Direct Atomic-Level Insight into the Active Sites of a High-Performance PGM-Free ORR Catalyst. *Science (80-.).* **2017**, *357* (6350), 479–484. https://doi.org/10.1126/science.aan2255.

(72) Rebarchik, M.; Bhandari, S.; Kropp, T.; Mavrikakis, M. How Noninnocent Spectator Species Improve the Oxygen Reduction Activity of Single-Atom Catalysts: Microkinetic Models from First-Principles Calculations. *ACS Catal.* **2020**, *10* (16), 9129–9135. https://doi.org/10.1021/acscatal.0c01642.

(73) Jurca, T.; Farghal, A.; Lin, P.-H.; Korobkov, I.; Murugesu, M.; Richeson, D. S. Single-Molecule Magnet Behavior with a Single Metal Center Enhanced through Peripheral Ligand Modifications. *J. Am. Chem. Soc.* **2011**, *133* (40), 15814–15817. https://doi.org/10.1021/ja204562m.

(74) Xiao, M.; Gao, L.; Wang, Y.; Wang, X.; Zhu, J.; Jin, Z.; Liu, C.; Chen, H.; Li, G.; Ge, J.; He, Q.; Wu, Z.; Chen, Z.; Xing, W. Engineering Energy Level of Metal Center: Ru Single-Atom Site for Efficient and Durable Oxygen Reduction Catalysis. *J. Am. Chem. Soc.* **2019**, *141* (50), 19800–19806. https://doi.org/10.1021/jacs.9b09234.

(75) Zhang, C.; Sha, J.; Fei, H.; Liu, M.; Yazdi, S.; Zhang, J.; Zhong, Q.; Zou, X.; Zhao, N.; Yu, H.; Jiang, Z.; Ringe, E.; Yakobson, B. I.; Dong, J.; Chen, D.; Tour, J. M. Single-Atomic Ruthenium Catalytic Sites on Nitrogen-Doped Graphene for Oxygen Reduction Reaction in Acidic Medium. *ACS Nano* **2017**, *11* (7), 6930–6941. https://doi.org/10.1021/acsnano.7b02148.

(76) He, Y.; Shi, Q.; Shan, W.; Li, X.; Kropf, A. J.; Wegener, E. C.; Wright, J.; Karakalos, S.; Su, D.; Cullen, D. A.; Wang, G.; Myers, D. J.; Wu, G. Dynamically Unveiling Metal – Nitrogen Coordination during Thermal Activation to Design High-Efficient Atomically Dispersed CoN 4 Active Sites. *Angew. Chem. Int. Ed. Engl.* **2021**, *60* (17), 9602–9612. https://doi.org/10.1002/ange.202017288.

(77) Li, X.; Surkus, A. E.; Rabeah, J.; Anwar, M.; Dastigir, S.; Junge, H.; Brückner, A.; Beller, M. Cobalt Single-Atom Catalysts with High Stability for Selective Dehydrogenation of Formic Acid. *Angew. Chemie - Int. Ed.* **2020**, *59* (37), 15849–15854. https://doi.org/10.1002/anie.202004125.

(78) Martinez, U.; Holby, E. F.; Babu, S. K.; Artyushkova, K.; Lin, L.; Choudhury, S.; Purdy, G. M.; Zelenay, P. Experimental and Theoretical Trends of PGM-Free Electrocatalysts for the Oxygen Reduction Reaction with Different Transition Metals. *J. Electrochem. Soc.* **2019**, *166* (7), F3136–F3142. https://doi.org/10.1149/2.0201907jes.

(79) Li, J.; Chen, M.; Cullen, D. A.; Hwang, S.; Wang, M.; Li, B.; Liu, K.; Karakalos, S.;

Lucero, M.; Zhang, H.; Lei, C.; Xu, H.; Sterbinsky, G. E.; Feng, Z.; Su, D.; More, K. L.; Wang, G.; Wang, Z.; Wu, G. Atomically Dispersed Manganese Catalysts for Oxygen Reduction in Proton-Exchange Membrane Fuel Cells. *Nat. Catal.* **2018**, *1* (12), 935–945. https://doi.org/10.1038/s41929-018-0164-8.

(80) Peng, H.; Liu, F.; Liu, X.; Liao, S.; You, C.; Tian, X.; Nan, H.; Luo, F.; Song, H.; Fu, Z.; Huang, P. Effect of Transition Metals on the Structure and Performance of the Doped Carbon Catalysts Derived From Polyaniline and Melamine for ORR Application. *ACS Catal.* **2014**, *4* (10), 3797–3805. https://doi.org/10.1021/cs500744x.

(81) Holst-Olesen, K.; Silvioli, L.; Rossmeisl, J.; Arenz, M. Enhanced Oxygen Reduction Reaction on Fe/N/C Catalyst in Acetate Buffer Electrolyte. *ACS Catal.* **2019**, *9* (4), 3082–3089. https://doi.org/10.1021/acscatal.8b04609.

(82) Gao, J.; Yang, H. bin; Huang, X.; Hung, S. F.; Cai, W.; Jia, C.; Miao, S.; Chen, H. M.; Yang, X.; Huang, Y.; Zhang, T.; Liu, B. Enabling Direct H2O2 Production in Acidic Media through Rational Design of Transition Metal Single Atom Catalyst. *Chem* **2020**, *6* (3), 658–674. https://doi.org/10.1016/j.chempr.2019.12.008.

(83) Geng, Z.; Liu, Y.; Kong, X.; Li, P.; Li, K.; Liu, Z.; Du, J.; Shu, M.; Si, R.; Zeng, J. Achieving a Record-High Yield Rate of 120.9 MgNH3mgcat.−1h−1 for N2 Electrochemical Reduction over Ru Single-Atom Catalysts. *Adv. Mater.* **2018**, *30* (40), 2–7. https://doi.org/10.1002/adma.201803498.

(84) Wan, H.; Jensen, A. W.; Escudero-Escribano, M.; Rossmeisl, J. Insights in the Oxygen Reduction Reaction: From Metallic Electrocatalysts to Diporphyrins. *ACS Catal.* **2020**, *10* (11), 5979–5989. https://doi.org/10.1021/acscatal.0c01085.

(85) Varela, A. S.; Ju, W.; Bagger, A.; Franco, P.; Rossmeisl, J.; Strasser, P. Electrochemical Reduction of CO2 on Metal-Nitrogen-Doped Carbon Catalysts. *ACS Catal.* **2019**, *9* (8), 7270–7284. https://doi.org/10.1021/acscatal.9b01405.

(86) Wang, J.; Huang, Z.; Liu, W.; Chang, C.; Tang, H.; Li, Z.; Chen, W.; Jia, C.; Yao, T.; Wei, S.; Wu, Y.; Li, Y. Design of N-Coordinated Dual-Metal Sites: A Stable and Active Pt-Free Catalyst for Acidic Oxygen Reduction Reaction. *J. Am. Chem. Soc.* **2017**, *139* (48), 17281–17284. https://doi.org/10.1021/jacs.7b10385.

(87) Wan, H.; Jiao, Y.; Bagger, A.; Rossmeisl, J. Three-Dimensional Carbon Electrocatalysts for CO2or CO Reduction. *ACS Catal.* **2021**, *11* (2), 533–541. https://doi.org/10.1021/acscatal.0c04878.

For Table of Contents Only